The Astrophysical Journal, 980:12 (21pp), 2025 February 10 https://doi.org/10.3847/1538-4357/ad9d0e

A SPectroscopic Survey of Biased Halos in the Reionization Era (ASPIRE): Spectroscopically Complete Census of Obscured Cosmic Star Formation Rate Density at $z = 4$–6

Fengwu Sun[1], Feige Wang[2,3], Jinyi Yang[2,3], Jaclyn B. Champagne[3], Roberto Decarli[4], Xiaohui Fan[3], Eduardo Bañados[5], Zheng Cai[6], Luis Colina[7], Eiichi Egami[3], Joseph F. Hennawi[8,9], Xiangyu Jin[3], Hyunsung D. Jun[10,11], Yana Khusanova[12], Mingyu Li[6], Zihao Li[13,14], Xiaojing Lin[6,3], Weizhe Liu[3], Romain A. Meyer[15], Maria A. Pudoka[3], George H. Rieke[3], Yue Shen[16,17], Wei Leong Tee[3], Bram Venemans[9], Fabian Walter[18], Yunjing Wu[6], Huanian Zhang[19], and Siwei Zou[6,20]

[1] Center for Astrophysics | Harvard & Smithsonian, 60 Garden Street, Cambridge, MA 02138, USA; fengwu.sun@cfa.harvard.edu
[2] Department of Astronomy, University of Michigan, 1085 S. University Avenue, Ann Arbor, MI 48109, USA
[3] Steward Observatory, University of Arizona, 933 N Cherry Avenue, Tucson, AZ 85721, USA
[4] INAF–Osservatorio di Astrofisica e Scienza dello Spazio, via Gobetti 93/3, I-40129, Bologna, Italy
[5] Max Planck Institut für Astronomie, Königstuhl 17, D-69117, Heidelberg, Germany
[6] Department of Astronomy, Tsinghua University, Beijing 100084, People's Republic of China
[7] Centro de Astrobiología (CAB), CSIC-INTA, Ctra. deAjalvir km 4, Torrejón de Ardoz, E-28850, Madrid, Spain
[8] Department of Physics, University of California, Santa Barbara, CA 93106-9530, USA
[9] Leiden Observatory, Leiden University, Niels Bohrweg 2, NL-2333 CA Leiden, Netherlands
[10] Department of Physics, Northwestern College, 101 7th Street SW, Orange City, IA 51041, USA
[11] School of Physics, Korea Institute for Advanced Study, 85 Hoegiro, Dongdaemun-gu, Seoul 02455, Republic of Korea
[12] Max-Planck-Institut für Astronomie, Königstuhl 17, D-69117 Heidelberg, Germany
[13] Cosmic Dawn Center (DAWN), Denmark
[14] Niels Bohr Institute, University of Copenhagen, Jagtvej 128, DK-2200 Copenhagen N, Denmark
[15] Department of Astronomy, University of Geneva, Chemin Pegasi 51, 1290 Versoix, Switzerland
[16] Department of Astronomy, University of Illinois at Urbana-Champaign, Urbana, IL 61801, USA
[17] National Center for Supercomputing Applications, University of Illinois at Urbana-Champaign, Urbana, IL 61801, USA
[18] Max Planck Institute for Astronomy, Königstuhl 17, D-69117 Heidelberg, Germany
[19] Department of Astronomy, Huazhong University of Science and Technology, Wuhan, Hubei 430074, People's Republic of China
[20] Chinese Academy of Sciences South America Center for Astronomy, National Astronomical Observatories, CAS, Beijing 100101, People's Republic of China

Received 2024 August 26; revised 2024 November 17; accepted 2024 December 8; published 2025 January 30

Abstract

We present a stringent measurement of the dust-obscured star formation rate density (SFRD) at $z = 4$–6 from the ASPIRE JWST Cycle-1 medium and ALMA Cycle-9 large program. We obtained JWST/NIRCam grism spectroscopy and ALMA 1.2 mm continuum map along 25 independent quasar sightlines, covering a total survey area of $\sim$35 arcmin^2 where we search for dusty star-forming galaxies (DSFGs) at $z = 0$–7. We identify eight DSFGs in seven fields at $z = 4$–6 through the detection of Hα or [O III] λ5008 lines, including fainter lines such as Hβ, [O III] λ4960, [N II] λ6585, and [S II] $\lambda\lambda$6718,6733 for six sources. With this spectroscopically complete DSFG sample at $z = 4$–6 and negligible impact from cosmic variance (shot noise), we measure the infrared luminosity function (IRLF) down to $L_{\rm IR} \sim 2 \times 10^{11}\,L_\odot$. We find flattening of IRLF at $z = 4$–6 towards the faint end (power-law slope $\alpha = 0.59^{+0.39}_{-0.45}$). We determine the dust-obscured cosmic SFRD at this epoch to be $\log[\rho_{\rm SFR,IR}/(M_\odot\ {\rm yr}^{-1}\,{\rm Mpc}^{-3})] = -1.52^{+0.14}_{-0.13}$. This is significantly higher than previous determinations using ALMA data in the Hubble Ultra Deep Field, which is void of DSFGs at $z = 4$–6 because of strong cosmic variance (shot noise). We conclude that the majority (66% ± 7%) of cosmic star formation at $z \sim 5$ is still obscured by dust. We also discuss the uncertainty of SFRD propagated from far-IR spectral energy distribution and IRLF at the bright end, which will need to be resolved with future ALMA and JWST observations.

Unified Astronomy Thesaurus concepts: James Webb Space Telescope (2291); Starburst galaxies (1570); High-redshift galaxies (734); Luminous infrared galaxies (946); Galaxy evolution (594)

1. Introduction

It is now clear that the cosmic star formation history peaked at around a redshift of two (see review by P. Madau & M. Dickinson 2014). Before this so-called "cosmic noon," a decline of unobscured cosmic star formation rate densities (SFRD) toward higher redshifts has been suggested by Hubble Space Telescope (HST) observations at rest-frame ultraviolet (UV) wavelengths (e.g., R. J. Bouwens et al. 2015; S. L. Finkelstein et al. 2015; R. Bouwens et al. 2020). However, the measurements of dust-obscured SFRD at infrared (IR) to millimeter wavelengths were much more challenging and uncertain. Although exciting constraints have been placed with multiple telescopes including Herschel (e.g., D. Burgarella et al. 2013; C. Gruppioni et al. 2013; M. Rowan-Robinson et al. 2016; D. Liu et al. 2018; L. Wang et al. 2019), the James Clerk Maxwell Telescope (JCMT; e.g., M. P. Koprowski et al. 2017; C.-F. Lim et al. 2020), and the Atacama Large Millimeter/submillimeter Array (ALMA; e.g., J. S. Dunlop et al. 2017; R. Bouwens et al. 2020; C. Gruppioni et al. 2020; Y. Khusanova et al. 2021; J. A. Zavala et al. 2021;

S. Fujimoto et al. 2023; B. Magnelli et al. 2024; A. Traina et al. 2024), most existing studies rely on a long list of assumptions, including the shape of the infrared luminosity function (IRLF), the mid-to-far-IR spectral energy distribution (SED), and also photometric redshifts that are strongly degenerate with the stellar age and dust attenuation.

One of the most critical uncertainties is from photometric redshifts ($z_{\rm phot}$). The vast majority of dusty star-forming galaxies (DSFGs) are found at $z \simeq$ 2–3 (e.g., see reviews by C. M. Casey et al. 2014a; J. A. Hodge & E. da Cunha 2020). Therefore, it is usually very challenging to differentiate true DSFGs at $z > 4$ from lower-redshift "interlopers" with large $z_{\rm phot}$ error (e.g., see the recent dispute regarding COSBO-7 at $z_{\rm phot} > 7$ but spectroscopic redshift $z_{\rm spec} = 2.625$; C. Ling et al. 2024, S. Jin et al. 2024a). Many of these DSFGs at $z_{\rm phot} \gtrsim 4$ are totally dust-obscured at HST wavelengths, and therefore also known as "HST-dark," "NIR-dark," "*H*-dropout," or "*H*-faint" galaxies (e.g., J. S. Huang et al. 2011; E. da Cunha et al. 2015; J. M. Simpson et al. 2015; S. Fujimoto et al. 2016; M. Franco et al. 2018; B. Alcalde Pampliega et al. 2019; T. Wang et al. 2019; Y. Yamaguchi et al. 2019; F. Sun et al. 2021; M. Talia et al. 2021; A. Enia et al. 2022; C. Gómez-Guijarro et al. 2022; V. Kokorev et al. 2022; S. M. Manning et al. 2022; M. Y. Xiao et al. 2023; A. Tsujita et al. 2024), including a certain amount of galaxies that are only detected with ALMA (e.g., R. Decarli et al. 2017; C. Mazzucchelli et al. 2019; B. P. Venemans et al. 2019; C. C. Williams et al. 2019; Y. Fudamoto et al. 2021; F. Wang et al. 2023). Therefore, it is very challenging to obtain secure redshifts of these galaxies through ground-based optical/near-IR spectroscopy.

At $z \gtrsim 4$, luminous infrared galaxies (LIRG; IR luminosity $10^{11}\,L_\odot \leqslant L_{\rm IR} < 10^{12}\,L_\odot$) and the bulk of ultra-luminous infrared galaxies (ULIRG; $10^{12}\,L_\odot \leqslant L_{\rm IR} < 10^{13}\,L_\odot$) are below the Herschel/SPIRE confusion noise limit at 250–500 μm (e.g., H. T. Nguyen et al. 2010), making it difficult to tightly constrain redshifts through far-IR SED except for extraordinarily luminous and/or gravitationally lensed galaxies (e.g., D. A. Riechers et al. 2013; T. D. Rawle et al. 2014; F. Sun et al. 2022). Large millimeter interferometers (e.g., ALMA, the Plateau de Bure Interferometer (PdBI), and its successor, the Northern Extended Millimeter Array, (NOEMA)) can obtain redshifts of distant DSFGs through CO and [C II] λ158 μm line scans. However, such types of observations are time-consuming for high-redshift LIRGs and ULIRGs (e.g., 8.3 hr on-source for the ALMA CO scan of MAMBO-9 at $z_{\rm spec} = 5.85$ with $L_{\rm IR} \sim 4 \times 10^{12}\,L_\odot$; C. M. Casey et al. 2019; S. Jin et al. 2019), again with exceptions for extraordinarily luminous sources at observed $L_{\rm IR} \gtrsim 10^{13}\,L_\odot$ (e.g., A. Weiß et al. 2013; M. L. Strandet et al. 2016; C. Reuter et al. 2020; C.-C. Chen et al. 2022).

Without spectroscopic redshifts, it is very challenging to securely select a sample of DSFGs at $z > 4$, directly measure their IRLF and accurately determine the obscured SFRD. For example, based on serendipitous (sub)millimeter continuum sources discovered by Cycle-5 "ALMA Large Program to INvestigate CII at Early Times" (ALPINE; O. Le Fèvre et al. 2020), C. Gruppioni et al. (2020) found that the obscured SFRD remains almost constant across $z \simeq 2-6$. This is in great contrast to the results based on the Cycle-4 large program "ALMA Spectroscopic Survey in the Hubble Ultra Deep Field (HUDF)" (ASPECS; F. Walter et al. 2016), where no DSFGs at $z > 4$ was blindly discovered with deep 1 mm and 3 mm survey of the HUDF (M. Aravena et al. 2020; also J. S. Dunlop et al. 2017; B. Hatsukade et al. 2018). Alternative methods have been developed to infer obscured SFRD through the relation between infrared excess (IRX $= L_{\rm IR}/L_{\rm UV}$, i.e., the IR-to-UV luminosity ratio) and UV continuum slope $\beta_{\rm UV}$ (e.g., G. R. Meurer et al. 1999) or stellar mass $M_{\rm star}$ (e.g., R. Bouwens et al. 2020; Y. Khusanova et al. 2021; H. S. B. Algera et al. 2023; B. Magnelli et al. 2024), or a backward modeling approach that could infer the redshift evolution of IRLF (and thus obscured SFRD) through (sub)millimeter number counts (C. M. Casey et al. 2018a, 2018b; J. A. Zavala et al. 2021). Nevertheless, the obscured SFRD at $z \sim 5$ measured based on ASPECS (e.g., R. Bouwens et al. 2020; J. A. Zavala et al. 2021) data is still lower than that measured with ALPINE by $\sim$1 dex (C. Gruppioni et al. 2020).

Most recently, direct measurements through the ALMA Cycle-6 large program "ALMA Lensing Cluster Survey" (ALCS; K. Kohno et al. 2023) suggest that the obscured SFRD at $z \sim 5$ is between those inferred through the ALPINE and ASPECS programs (S. Fujimoto et al. 2023). Despite significant advance made with ALCS in probing DSFGs toward sub-LIRG luminosity ($L_{\rm IR} < 10^{11}\,L_\odot$) and reducing cosmic variance (shot noise) through 33 lensing cluster fields, caution is still necessary, as the ALCS sample of DSFGs at $z > 4$ is not yet spectroscopically complete.

JWST (J. P. Gardner et al. 2023) provides unprecedented opportunities to obtain near-IR spectroscopy of DSFGs at high redshifts. Specifically, with NIRCam wide-field slitless spectroscopy (WFSS) at 2.4–5.0 μm (M. J. Rieke et al. 2023), it is now possible to obtain near-IR spectra of all galaxies that enter the field of view (FoV; up to $\sim$9 arcmin^2). It has been clear from JWST Cycle-1 programs that Hα lines from HST-dark DSFGs at $z > 5$ can be easily detected with NIRCam WFSS with an on-source integration time of 1–2 hr (e.g., F. Sun et al. 2024; C. C. Williams et al. 2024; M. Xiao et al. 2024; T. Herard-Demanche et al. 2025). This promises a highly complete spectroscopic survey of dust-obscured star formation history toward the Epoch of Reionization.

In this work, we present a stringent measurement of IRLF and obscured SFRD at $z = 4$–6 through the ASPIRE JWST Cycle-1 medium and ALMA Cycle-9 large program (F. Wang et al. 2024, in preparation). Through ALMA and JWST spectroscopic survey of DSFGs over 25 independent quasar sightlines, we discovered eight DSFGs at $z_{\rm spec} = 4-6$ down to a 1.2 mm flux density of $S_{\rm 1.2\,mm} \sim 0.15$ mJy. We describe the observations and data processing techniques in Section 2, and present the redshift confirmation and analyses of their physical properties in Section 3. We then study their dust obscuration, contribution to the 1.2 mm number count, IRLF, and obscured SFRD in Section 4. Further implications and cautions are discussed in Section 5. Our conclusions are summarized in Section 6.

Throughout this work, we assume a flat ΛCDM cosmology with $H_0 = 70$ km s^{-1} Mpc^{-1}, $\Omega_{\rm M} = 0.3$, and $\sigma_8 = 0.8$. An AB magnitude system (J. B. Oke & J. E. Gunn 1983) is adopted to describe source brightness in the optical and near-IR. We also assume a G. Chabrier (2003) initial mass function. We define the IR luminosity ($L_{\rm IR}$) as the integrated luminosity over a rest-frame wavelength range from 8 to 1000 μm.

2. Observation and Data Reduction

2.1. JWST/NIRCam

ASPIRE started as a 62 hr JWST Cycle-1 medium program (PI: F. Wang; Program ID: 2078). With the powerful NIRCam WFSS observing mode, ASPIRE observed 25 luminous

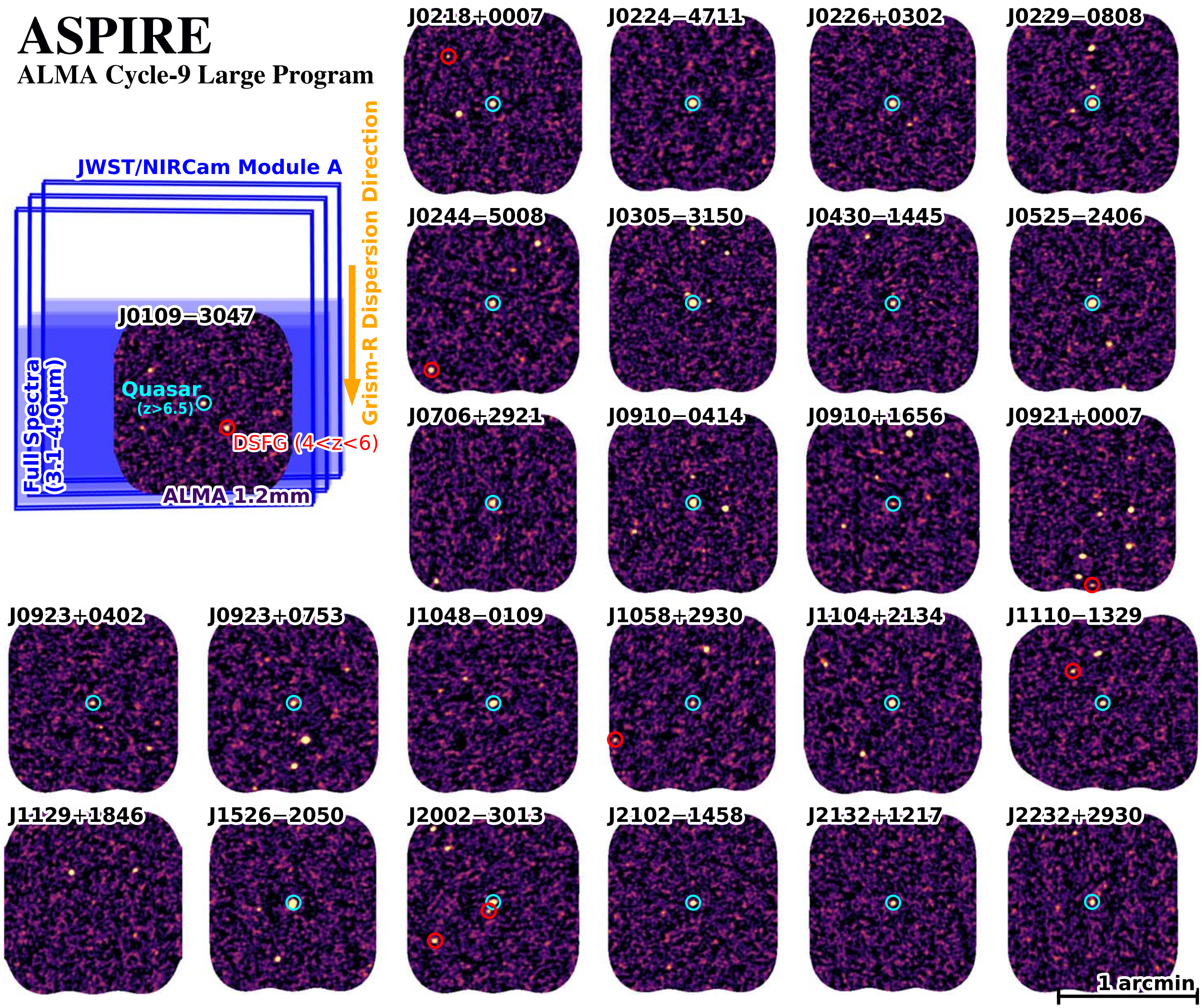

Figure 1. The 1.2 mm continuum images of 25 quasar fields obtained by the ASPIRE–ALMA Cycle-9 large program. In the top left panel, we highlight the design of JWST/NIRCam and ALMA observations. The whole ALMA 1.2 mm continuum imaging mosaics (*uv*-tapered with FWHM = 1″) are within the full spectral ($\lambda = 3.1$–4.0 μm with F356W filter) coverage region of NIRCam module A, as indicated by the blue shaded region. The quasar J0109–3047 ($z = 6.791$; cyan circle) is located in the center of ALMA footprint, and one DSFG (J0109m3047.C02 at $z = 5.549$) is also highlighted with a red circle. The position angle of the NIRCam WFSS observation is 270° for the J0109 field, and therefore the grism-R dispersion direction is almost from north to south, as indicated by the orange arrow. Note that the dispersion direction depends on the JWST/NIRCam PA and varies from field to field. ALMA 1.2 mm continuum images of all the other 24 fields are also displayed. Quasars with continuum detection ($z = 6.5$–6.8) and spectroscopically confirmed DSFGs at $z = 4$–6 are highlighted in cyan and red circles, respectively. Many DSFGs at other redshifts are also detected with ALMA but not highlighted in this figure.

quasars at $z = 6.5-6.8$ through NIRCam grism WFSS in the F356W filter (3.1–4.0 μm) and imaging in the F115W, F200W, and F356W filters (1–4 μm). The observational design of ASPIRE JWST program will be presented by F. Wang et al. (2024, in preparation; see also F. Wang et al. 2023; J. Yang et al. 2023). The primary science goal of ASPIRE is to detect companion galaxies at the quasar redshifts through [O III] $\lambda\lambda$4960,5008 and Hβ lines, and therefore answer whether the most massive black holes in the early Universe reside in the most massive dark matter halos (F. Wang et al. 2023). ASPIRE has also enabled a large number of other scientific investigations including supermassive black hole mass measurements (J. Yang et al. 2023), the morphology of quasar host galaxies and outflows (J. Yang et al. 2024, in preparation), the environmental impact on galaxy properties and evolution history at $z \sim 6.5$ (J. B. Champagne et al. 2024b, 2024a), the connection between intergalactic medium (IGM) opacity and galaxies at $z \sim 6$ (X. Jin et al. 2024), and the metal enrichment of circumgalactic medium (CGM) at $z \simeq 4-6$ (Y. Wu et al. 2023; S. Zou et al. 2024).

In all of the 25 quasar fields observed with ASPIRE, the NIRCam WFSS on-source integration time with the F356W filter is 2834s. Grism R was used, which disperses light along the row (horizontal) direction of the detector at a spectral resolution of $R \simeq 1300$–1600. The quasar was placed in the full spectral coverage region in module A (see F. Wang et al. 2023 and Figure 1) because of higher throughput (M. J. Rieke et al. 2023). During the NIRCam WFSS exposure through the long-wavelength (LW) channel, the short-wavelength (SW) channel of NIRCam obtained direct imaging observation with the F200W filter. After the WFSS exposure, direct imaging observations were obtained in the F115W and F356W filters through SW and LW channel, respectively, and the exposure time is 1417 s for both filters.

ASPIRE NIRCam data reduction has been described by F. Wang et al. (2023) and J. Yang et al. (2023), and will be described in full detail by F. Wang et al. (2024, in preparation). Here, we only briefly describe the key steps adopted in the data processing routine.

The NIRCam imaging data were processed based on the JWST calibration pipeline (H. Bushouse et al. 2023) `v1.10.2` with the reference file `jwst_1080.pmap` (including JWST Cycle-1 NIRCam flux calibrations). Customized steps included the $1/f$ noise subtraction along both the row and column directions on the stage-1 data products (`_rate` files). The sky background was determined iteratively and subtracted after masking detected sources in the images. The world coordinate systems (WCS) of all images are aligned to Gaia DR3 (Gaia Collaboration et al. 2023) or the DESI Legacy Imaging Survey (A. Dey et al. 2019) if not enough Gaia stars are found within the FoV. The flux-calibrated, WCS-registered and background-subtracted stage-2 data products (`_cal` files) were then passed through the stage-3 pipeline to create mosaicked images in each band. The final mosaicked images in each band were produced with fixed pixel size $0\farcs031$ (for F115W and F200W; native SW pixel size) and $0\farcs0315$ (for F356W; half of native LW pixel size) with `pixfrac = 0.8`.

The NIRCam WFSS data were processed using a combination of the JWST calibration pipeline `v1.10.2` (H. Bushouse et al. 2023) and customized scripts. Starting from stage-1 data products, we subtract $1/f$ noise pattern along the column direction (i.e., orthogonal to the grism dispersion direction). The grism images were then flat-fielded and assigned WCS information. We also subtracted master median background models from the processed images. After that, the astrometric offsets were measured between the simultaneous SW exposure and the fully calibrated F356W image mosaics, and the offsets were applied to the tracing and dispersion models (based on commissioning data; F. Sun et al. 2023). We then extracted 2D spectra of sources from each individual grism exposure, and the data were coadded into 2D spectra resampled into a common wavelength (9.8 Å pixel^{-1}; i.e., native dispersion) and spatial grids following the histogram 2D technique in the PYPEIT software (J. Prochaska et al. 2020). We then extracted 1D spectra from the coadded 2D spectra using both optimal (K. Horne 1986) and boxcar extraction algorithms. Because NIRCam WFSS mode effectively obtains spectra of all sources entering its FoV, contaminants are often seen in 2D and 1D spectra. In this work, we modeled and subtracted the continuum emission (mostly from contaminants) in 1D spectra through spline interpolation after masking the emission-line wavelength range ($|\Delta\lambda_{\rm obs}|\leqslant 0.05\,\mu$m). We also visually inspected 2D and 1D spectra, as well as JWST images, to identify and reject emission-line contaminants.

2.2. ALMA

ALMA 1.2 mm mosaics of all 25 ASPIRE quasar fields were obtained through a 100 hr ALMA Cycle-9 large program (PI: F. Wang; Program ID: 2022.1.01077.L). In each of the ALMA band-6 mosaics, we tuned the central frequency of the lower sideband as the [C II] line frequency at the quasar redshift (min–median–max: 243.0–247.9–252.9 GHz). Two 1.875–GHz spectral windows were placed to cover the –2200 ∼ +2200 km s^{-1} velocity range around the quasar redshift, with the primary goal being to blindly detect [C II] emitters at quasar vicinity and measure the Mpc-scale clustering of [C II] emitters around these quasars. Two more spectral windows were placed in the upper sideband to increase the continuum sensitivity, and the final effective frequencies of continuum images are 250.6–255.6–260.6 GHz (min–median–max). As illustrated in Figure 1, in each quasar field, we map the $\sim 1\farcm2 \times 1\farcm1$ region centered on the quasar with ∼ 23 Nyquist-sampled ALMA 12 m pointings. The ALMA footprints are covered by the full spectral coverage region of NIRCam WFSS at 3.1–4.0 μm, allowing us to search for emission lines from these ALMA sources.

ASPIRE–ALMA observations were conducted from 2022 October 14 to 2023 February 14 through C-2/3 configuration. The typical angular resolution of ALMA observation is $\sim 0\farcs65$. The total survey area of the ASPIRE–ALMA program is 34.9 arcmin^2 above a primary beam response limit of 0.25 as adopted in this paper.

We reduced all ALMA data with the standard CASA `v6.4.1.12` pipeline (J. P. McMullin et al. 2007; CASA Team et al. 2022) for Cycle-9 data. Our data reduction started from raw ALMA science data models with the restoration of pipeline-calibrated, observatory-flagged data through `scriptForPI.py`. These calibrated measurement sets were then concatenated and imaged based on the North American ALMA imaging script template.[21] To avoid the artificial boost of continuum flux densities from [C II] emitters at quasar redshifts, we first flagged the spectral channels that have a velocity offset smaller than 500 km s^{-1} from the quasar [C II] line center. Noisy spectral channels caused by telluric absorption were also visually identified through command `plotms` and flagged from continuum imaging. We then split the measurement sets to a channel width of 125 MHz and obtained continuum imaging at both native ALMA resolution (Briggs weighting `robust = 0.5`, no *uv* tapering) and tapered resolution (`robust = 2.0`, *uv* tapered with a Gaussian kernel of FWHM = $1\farcs0$). The reduction with `robust = 0.5` weighting is to optimize the sensitivity for compact emission, and our trail suggests that the sensitivity is similar to that of naturally weighted (`robust = 2.0`, no *uv* tapering) imaging data products. At tapered resolutions, sources with extended structural profiles (FWHM $\gtrsim 1''$) can be detected at a higher signal-to-noise ratio (S/N) than that of a native-resolution image. The synthesized beam FWHM is $0\farcs65 \pm 0\farcs05$ and $1\farcs34 \pm 0\farcs05$ for native and tapered continuum image mosaics, respectively. The image mosaics were produced via the `tclean` command with a pixel size of $0\farcs12$. Since it exhibited accuracy comparable to that of manual-masking results in our trials, we adopted the automatic multi-threshold masking algorithm (A. A. Kepley et al. 2020) in order to save human labor for interactive masking. The continuum rms noises (before primary beam response correction) of our ALMA mosaics are 0.031 ± 0.004 mJy beam^{-1} and 0.034 ± 0.004 mJy beam^{-1} at native and tapered resolution, respectively.

ALMA continuum sources were identified on both native and tapered images using the simple `find_peaks` algorithm in PHOTUTILS (L. Bradley et al. 2024). The detailed statistics of

---

[21] https://github.com/aakepley/ALMAImagingScript

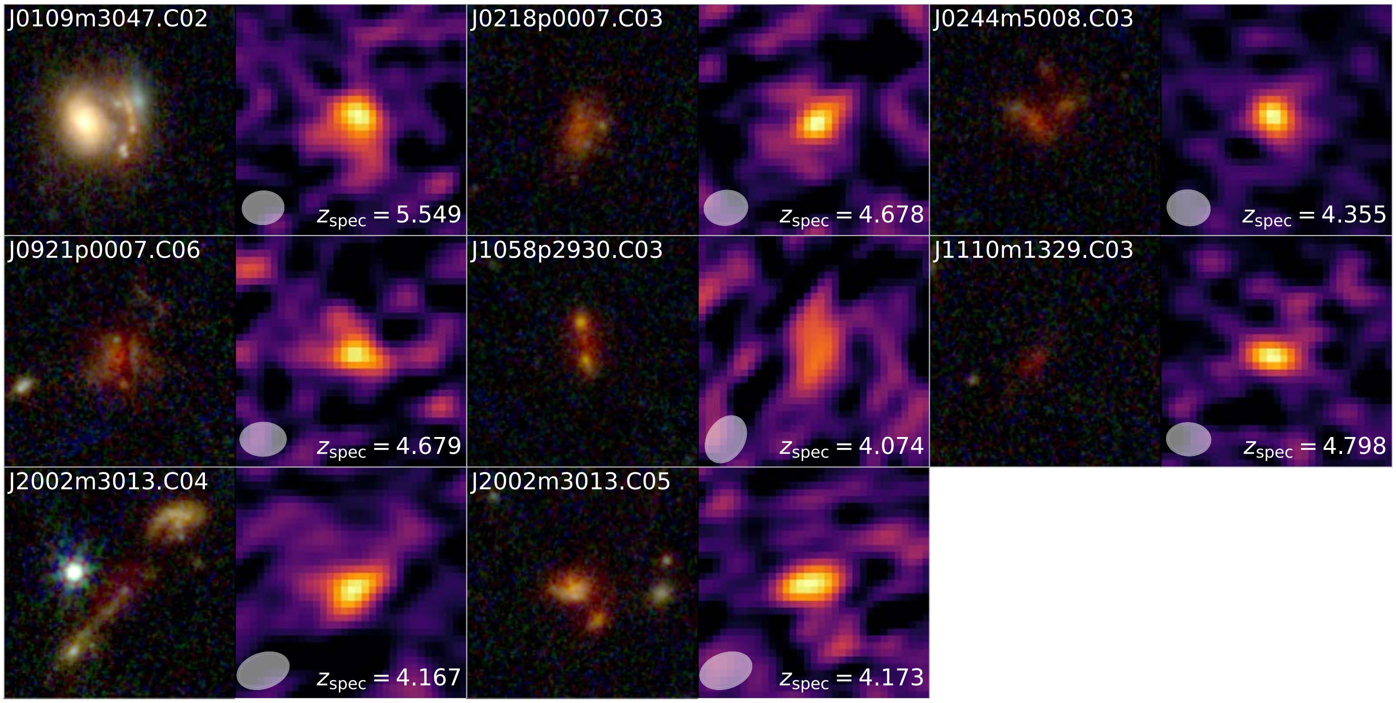

Figure 2. JWST NIRCam (red: F356W; green: F200W; blue: F115W) and ALMA 1.2 mm continuum images of DSFGs at $z = 4$–6 discovered with the ASPIRE survey. Image sizes are $4'' \times 4''$(north is up and east is left). Source IDs, spectroscopic redshifts, and ALMA beam sizes are indicated in the plots. Most sources appear red in JWST RGB images, indicating that they are highly dust-obscured galaxies at high redshifts. Note that J0109m3047.C02 is gravitationally lensed by the bright galaxy on the left (see Appendix A).

ALMA continuum sources at all redshifts will be presented by a forthcoming paper from the collaboration. We select ALMA continuum sources at signal-to-noise ratio $\mathrm{S/N} \geqslant 5$ in native images or $\mathrm{S/N} \geqslant 4$ in tapered images (i.e., similar to other ALMA Band-6 continuum surveys; e.g., S. Fujimoto et al. 2023), resulting in 138 nonrepeated peaks. From all ALMA images, we find that the most significant negative peak is at 5.01σ in native images and 5.04σ in tapered images, and above our detection threshold there are 1 and 20 negative peaks in the native ($\mathrm{S/N} \leqslant -5$) and tapered ($\mathrm{S/N} \leqslant -4$) images, respectively. Therefore, we visually inspected the JWST images of positive peaks that are less significant than the strongest negative peaks, and rejected 20 positive peaks at $\mathrm{S/N} = 4-5$ that do not show clear JWST counterparts within $0\farcs7$. The number of rejected positive peaks is the same as the number of negative peaks above our detection threshold, indicating that spurious continuum sources have been properly removed from our sample.

The final ASPIRE–ALMA continuum source sample includes 117 sources (primary beam response $\geqslant 0.25$) down to a flux density of $S_{1.2\mathrm{mm}} = 0.11$ mJy (median: 0.52 mJy). Among them, 23 sources are targeted quasars at $z = 6.5-6.8$, while quasar J0921+0007 ($z = 6.5646$; J. Yang et al. 2021) and the radio-loud quasar J1129+1846 ($z = 6.824$; E. Bañados et al. 2021) are below the ALMA continuum detection limit, as shown in Figure 1. After inspecting the JWST images of the remaining 94 sources, we classify all of them as DSFGs at cosmological distances.

3. Analyses

3.1. Spectroscopic Identification of DSFGs at z = 4–6

To obtain spectroscopic redshifts of the aforementioned 94 ALMA continuum sources (excluding targeted quasars), we extract the NIRCam grism spectra of their JWST counterparts. At 3.1–4.0 μm, we expect to detect emission lines including Paschen α (Paα) at $z = 0.7-1.1$, Paβ at $z = 1.5-2.1$, Paγ and He I λ10833 at $z = 1.9-2.7$, [S III] λ9533 at $z = 2.3-3.1$, [S III] λ9071 at $z = 2.5-3.5$, and most relevantly, Hα at $z = 3.8-5.0$ and [O III] λ5008 at $z = 5.3-6.9$.

We visually inspect the 2D and 1D grism spectra of all ALMA continuum sources, both before and after continuum subtraction, to identify potential emission lines. Our visual inspection, together with the ALMA [C II] line search (which will be presented in a forthcoming paper from the collaboration), yields 16 redshifts at $z = 3.8-6.8$ through Hα, [O III], or [C II] line detections. Six sources are at $z > 6$, and all of them are quasar companions ($z = 6.5-6.8$). At our redshift range of interest, $z = 4$–6, which is not affected by potential galaxy overdensities associated with quasars, we obtain redshifts for eight sources.

The JWST and ALMA images of these eight sources are displayed in Figure 2. All of these sources are highly secure detections in ALMA ($\mathrm{S/N} \geqslant 6.5$), and all of them have JWST counterparts detected in the F200W and F356W band. The relative astrometric error between JWST and ALMA images is $\lesssim 0\farcs1$. Most of these sources appear red (i.e., large F200W–F356W and F115W–F356W color) in the JWST RGB image, indicating that they are highly dust-obscured galaxies at high redshifts. These sources are also clearly resolved at the JWST wavelengths without showing bright point-like structure, indicating that they unlikely host unobscured active galactic nuclei (AGN). Detailed morphological study of ASPIRE DSFGs will be a focus of future work from the collaboration.

Figures 3 and 4 show the 2D and 1D NIRCam grism spectra of these eight sources, grouped by the confidence level of the redshifts.

We classify the redshifts of six sources as secure (confidence `conf=1`; Figure 3), as at least two spectral lines are detected

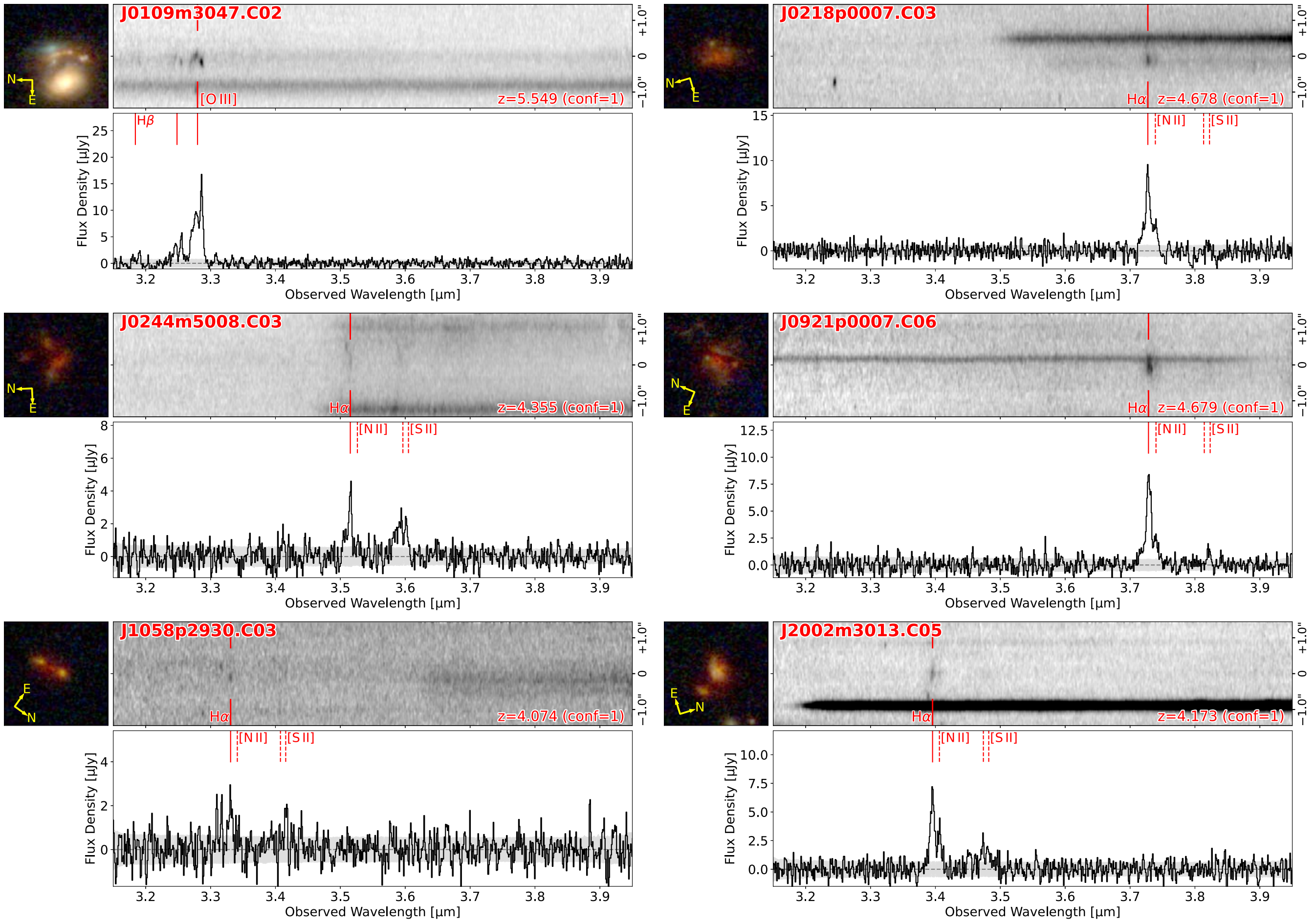

Figure 3. JWST NIRCam images, 2D spectra, and 1D spectra of six DSFGs with secure spectroscopic redshifts at 4−6 (`conf=1`). Note that the continuum emission (primarily from bright contaminating galaxies) is subtracted in 1D spectra but not in 2D spectra. NIRCam images are aligned along the dispersion direction (from left to right). Also note that the 2D spectra are compressed in the dispersion direction for display purposes. Primary emission lines (Hβ, [O III] $\lambda\lambda$4960,5008, Hα) are indicated with solid red lines, and other fainter lines ([N II] λ6585, [S II] $\lambda\lambda$6718,6733) are indicated with dashed red lines.

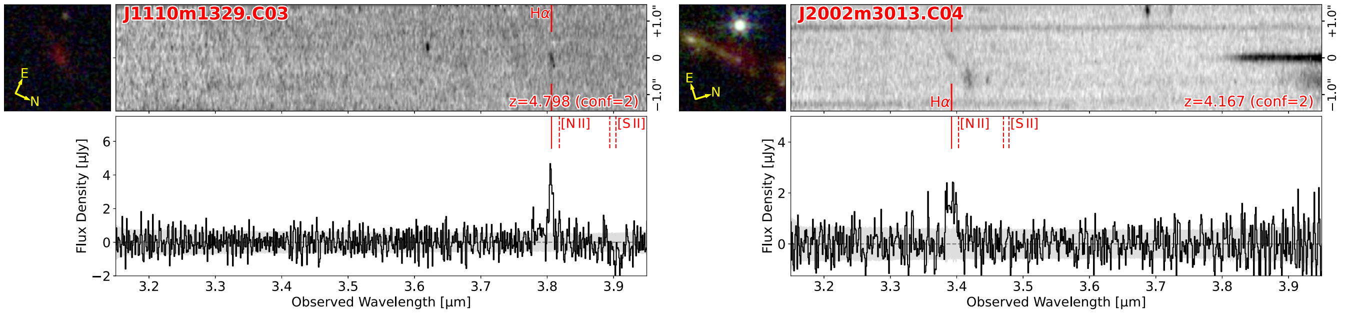

Figure 4. Same as Figure 3, but for two DSFGs with spectroscopic redshifts at 4–6 based on single emission line (`conf=2`).

(primary line at $\geqslant 5\sigma$ and secondary line at $\geqslant 3\sigma$). Among them, the highest-redshift source J0109m3047.C02 is detected in Hβ and [O III] $\lambda\lambda$4960, 5008, confirming the redshift at $z = 5.549$. We notice that J0109m3047.C02 is very close to a foreground galaxy ($z_{\rm phot} = 1.18 \pm 0.05$, separation $\sim 0\farcs8$). We estimate a gravitational lensing magnification of $\mu = 1.91 \pm 0.50$ at the centroid of ALMA continuum emission (see details in Appendix A). The other five sources in this group are detected in [N II] λ6585 and/or [S II] $\lambda\lambda$6718,6733 at 3σ significance at least, suggesting redshifts at $z = 4.07-4.68$.

The remaining two sources in Figure 4 only exhibit single-line detections in NIRCam grism spectra (confidence `conf=2`). Without the detection of a secondary line, it is hard to conclusively determine their nature, but we argue that these emission lines are most likely Hα at $z = 4.17$ and 4.80. We measure the emission-line flux from the continuum-subtracted 1D spectra through Gaussian-profile fitting, and subtract the line fluxes from the F356W Kron-aperture photometry. We then derive the equivalent widths (EWs) of these lines, finding large observed-frame EWs of 5240 ± 500 and 890 ± 270 Å for

Table 1

Photometric and Spectroscopic Properties of ASPIRE DSFGs at $z = 4$–6

ID	R.A. [deg]	Decl. [deg]	S/N	PB	$S_{1.2\ \mathrm{mm}}$ [mJy]	z_{spec}	conf	F115W [mag]	F200W [mag]	F356W [mag]	f_{line} [10^{-18} erg s^{-1} cm^{-2}]
J0109m3047.C02	17.46807	−30.79361	12.5	1.00	0.45 ± 0.04	5.549	1	26.01 ± 0.19	24.73 ± 0.05	23.94 ± 0.05	53.7 ± 1.2
J0218p0007.C03	34.70137	0.12652	6.5	0.88	0.28 ± 0.04	4.678	1	>26.70	25.26 ± 0.05	23.89 ± 0.05	15.8 ± 0.7
J0244m5008.C03	41.01580	−50.15628	13.4	0.51	1.03 ± 0.08	4.355	1	25.69 ± 0.35	25.80 ± 0.07	23.94 ± 0.05	5.9 ± 0.5
J0921p0007.C06	140.33569	0.11316	6.7	0.31	0.96 ± 0.14	4.679	1	>25.60	25.32 ± 0.07	23.76 ± 0.05	15.8 ± 0.7
J1058p2930.C03	164.54289	29.50715	6.6	0.31	0.84 ± 0.13	4.074	1	>27.49	25.58 ± 0.05	24.03 ± 0.05	3.6 ± 0.7
J1110m1329.C03	167.64528	−13.49222	9.1	0.99	0.38 ± 0.04	4.798	2	>27.20	27.62 ± 0.22	26.42 ± 0.05	6.0 ± 0.6
J2002m3013.C04	300.68137	−30.22729	11.2	0.76	0.61 ± 0.05	4.167	2	>27.14	25.77 ± 0.07	24.99 ± 0.05	7.6 ± 2.3
J2002m3013.C05	300.67392	−30.22369	7.0	1.00	0.29 ± 0.04	4.173	1	26.44 ± 0.14	24.94 ± 0.05	23.54 ± 0.05	13.2 ± 0.9

Notes. `S/N` is the maximum S/N measured from the ALMA native-resolution and *uv*-tapered maps. `PB` is the ALMA primary beam response. $S_{1.2\ \mathrm{mm}}$ is the ALMA continuum flux density measured from the peak of the *uv*-tapered map, corrected for primary beam response, and multiplied by a factor of 1.1 to match the flux densities measured from aperture and `CASA` image-plane fitting (`imfit`; Section 3.1). The uncertainty for the spectroscopic redshift is $\Delta z \sim 0.002$, mostly propagated from the wavelength calibration error of NIRCam WFSS. f_{line} is the [O III] λ5008 (for J0109m3047.C02) or Hα (for other sources) line fluxes measured from 1D NIRCam grism spectra. Lensing magnification is not corrected for J0109m3047.C02 (see Appendix A).

J1110m1329.C03 and J2002m3013.C04, respectively. Such large EWs are extremely hard to reproduce with lower-redshift Paschen or He I λ10833 lines, based on the analyses of F444W grism data of DSFGs in the GOODS-S field (FRESCO; P. A. Oesch et al. 2023; L. A. Boogaard et al. 2024; F. Sun 2024, private communication), and the most likely line solution is therefore Hα or [O III] λ5008. Therefore, we conclude the following:

1. *J1110m1329.C03.* The nondetection of a secondary line indicates that the detected line can only be Hα at $z = 4.798$, otherwise the [O III] λ4960 line would have been detected at $> 3\sigma$.
2. *J2002m3013.C04.* The wavelength of detected emission line of J2002m3013.C04 is very similar to the Hα wavelength of J2002m3013.C05 (velocity offset $\delta v = 350$ km s^{-1}) in the same quasar field, and other line emitter at similar wavelengths are also identified in the vicinity of J2002m3013.C04 (see the 2D spectrum). Therefore, J2002m3013.C04 ($z = 4.173$) is likely associated with a group of Hα emitters at $z = 4.17$.

J1110m1329.C03 and J2002m3013.C04 are the only two single-line emitters in the ASPIRE DSFG sample that are undetected in the F115W band ($< 3\sigma$) and thus likely reside at $z > 4$, similar to many photometrically selected DSFGs at $z \gtrsim 4$ through JWST imaging surveys (e.g., J. McKinney et al. 2023b, 2024; R. Gottumukkala et al. 2024; C. C. Williams et al. 2024). For all of the emission-line solutions above, we also examine the ALMA spectral cubes to make sure that none of them are misidentified [O III]+[C II] emitters around quasar redshifts. We also experiment with other line solutions, e.g., He I λ10833 and Paγ, and we find that these solutions do not match the observed wavelengths or strengths of emission-line complexes.

We notice that some of the emission lines in Figures 3 and 4 appear to be broad (FWHM $\gtrsim$ 1000 km s^{-1}). This is mostly because of morphological broadening with slitless spectroscopy, but not necessarily the presence of AGN. A galaxy with FWHM $\sim$ 0.″8 will exhibit a line width of $0.''8 \cdot (0.''063\ \mathrm{pixel}^{-1})^{-1}(0.98\ \mathrm{nm.pixel}^{-1})\,\lambda_{\mathrm{obs}}^{-1} c \sim 1000\ \mathrm{km\,s^{-1}}$ with NIRCam slitless spectroscopy, even without further consideration of instrumental or Doppler broadening. The presence (or absence) of broad-line AGN will need to be examined with further slit or integral-field spectroscopy.

Table 1 summarizes the photometric and spectroscopic information of these eight DSFGs at $z =$ 4–6. We construct the JWST detection image by coadding F200W and F356W images, create image segments for regions that have at least 10 continuous pixels detected at $\geqslant 5\sigma$, and then obtain aperture photometry using the Kron parameters `k=2.5` and `Rmin=1.2` in all JWST bands. The photometry of J0109m3047.C02 is obtained on the residual images with other foreground galaxies modeled and subtracted with GALFIT (C. Y. Peng et al. 2010; Appendix A). The photometric uncertainty is estimated from the sky background with a conservative noise floor of 5%, following the practice of the NIRCam guaranteed-time-observation team (e.g., S. Tacchella et al. 2023).

At the ALMA wavelength, we adopt the peak flux densities of sources in the uv-tapered images (f_{tap}) multiplied by a factor of 1.1. This is because we find that the scaled-up f_{tap} is systematically consistent with the flux densities measured with $r = 1''$ aperture (f_{aper}) and CASA image-plane fitting (`imfit`; f_{imfit}) in the native-resolution images, but with considerably smaller uncertainties. The scaling factor is also verified with the injection experiment detailed in Appendix B.

For Hα emitters, we measure the emission-line fluxes through multi-component Gaussian-profile fitting. For J0109m3047.C02 with complex morphological and thus line profiles, we integrate the 1D spectrum within 20 Å (rest-frame) from the line center to derive the line fluxes.

3.2. SED Modeling

We obtain physical SED modeling of eight ASPIRE DSFGs at $z =$ 4–6 using software CIGALE (S. Noll et al. 2009; M. Boquien et al. 2019). We use four-band NIRCam and ALMA photometry for the fitting. Because the rest-frame far-IR SEDs are only loosely constrained by ALMA photometry in one band, we have to rely on the energy-balance assumption with CIGALE to infer the IR luminosity and thus the obscured SFR. In Section 5.1, we discuss the validity of the energy-balance assumption and the impact from the uncertain dust temperature.

We assume a commonly used delayed-τ star formation history (SFH), in which SFR$(t) \propto t\exp(-t/\tau)$ and τ is the peak time of star formation. We allow the age of the main stellar population to be 10–500 Myr and τ to be 30–3000 Myr. An optional late starburst is allowed in the last 10 Myr of SFH, which could produce up to 20% of total stellar mass. We use the G. Bruzual & S. Charlot (2003) stellar population synthesis models, and allow a metallicity range of $0.4Z_{\odot}$–$Z_{\odot}$. We adopt a modified D. Calzetti et al. (2000) attenuation curve, and allow the variation of the power-law slope by ±0.3 and A_V effectively at 0–10. For simplicity, we assume the C. M. Casey (2012) mid-to-far-IR dust continuum model that could be parameterized by dust temperature (T_{dust}; flat prior at 30–50 K), dust emissivity (β_{em}; fixed at 1.8), and mid-IR power-law slope (α_{MIR}; fixed at 2.0). Although the C. M. Casey (2012) model does not include mid-IR polycyclic aromatic hydrocarbon (PAH) features, the inclusion of a mid-IR power-law slope can well reproduce the luminosity excess from PAHs from a comparison of widely used empirical SED templates (uncertainty $\lesssim$0.1 dex; e.g., R. Chary & D. Elbaz 2001; G. H. Rieke et al. 2009). Note that we do not include nebular emission in the SED modeling for simplicity. Instead, we subtract the identified emission-line fluxes (Hα, [O III], Hβ, [N II], and [S II]) from the F356W photometry, and perform the SED fitting for pure stellar and dust continuum. For J0109m3047.C02, we correct for the differential lensing magnification in the SED modeling (Appendix A).

Figure 5 shows the best-fit SED models of eight DSFGs in our sample, and the derived physical parameters are presented in Table 2. We observe a median stellar mass $\log(M_{\mathrm{star}}/M_{\odot}) = 10.3 \pm 0.2$ for sources in our sample, and the median IR luminosity is $\log(L_{\mathrm{IR}}/L_{\odot}) = 11.7 \pm 0.1$, i.e., comparable to LIRGs in the local Universe. We also derive the UV SFR for each source through the observed F115W flux density (rest-frame $\sim$ 2000 Å) and the conversion $\mathrm{SFR_{UV}}/(M_{\odot}\ \mathrm{yr}^{-1}) = 8.8 \times 10^{-29}\,L_{\mathrm{FUV}}/(\mathrm{erg\,s^{-1}\,Hz^{-1}})$ (per P. Madau & M. Dickinson (2014), but assuming a G. Chabrier (2003) IMF). Under the same IMF assumption, the conversion between IR luminosity and dust-obscured SFR is $\mathrm{SFR_{IR}}/(M_{\odot}\ \mathrm{yr}^{-1}) = 1.1 \times 10^{-10}\,L_{\mathrm{IR}}/L_{\odot}$, and the conversion between Hα luminosity and SFR is $\mathrm{SFR_{H\alpha}}/(M_{\odot}\ \mathrm{yr}^{-1}) = 5 \times 10^{-42}\,L_{\mathrm{H\alpha}}/(\mathrm{erg\,s^{-1}})$ (R. C. J. Kennicutt 1998).

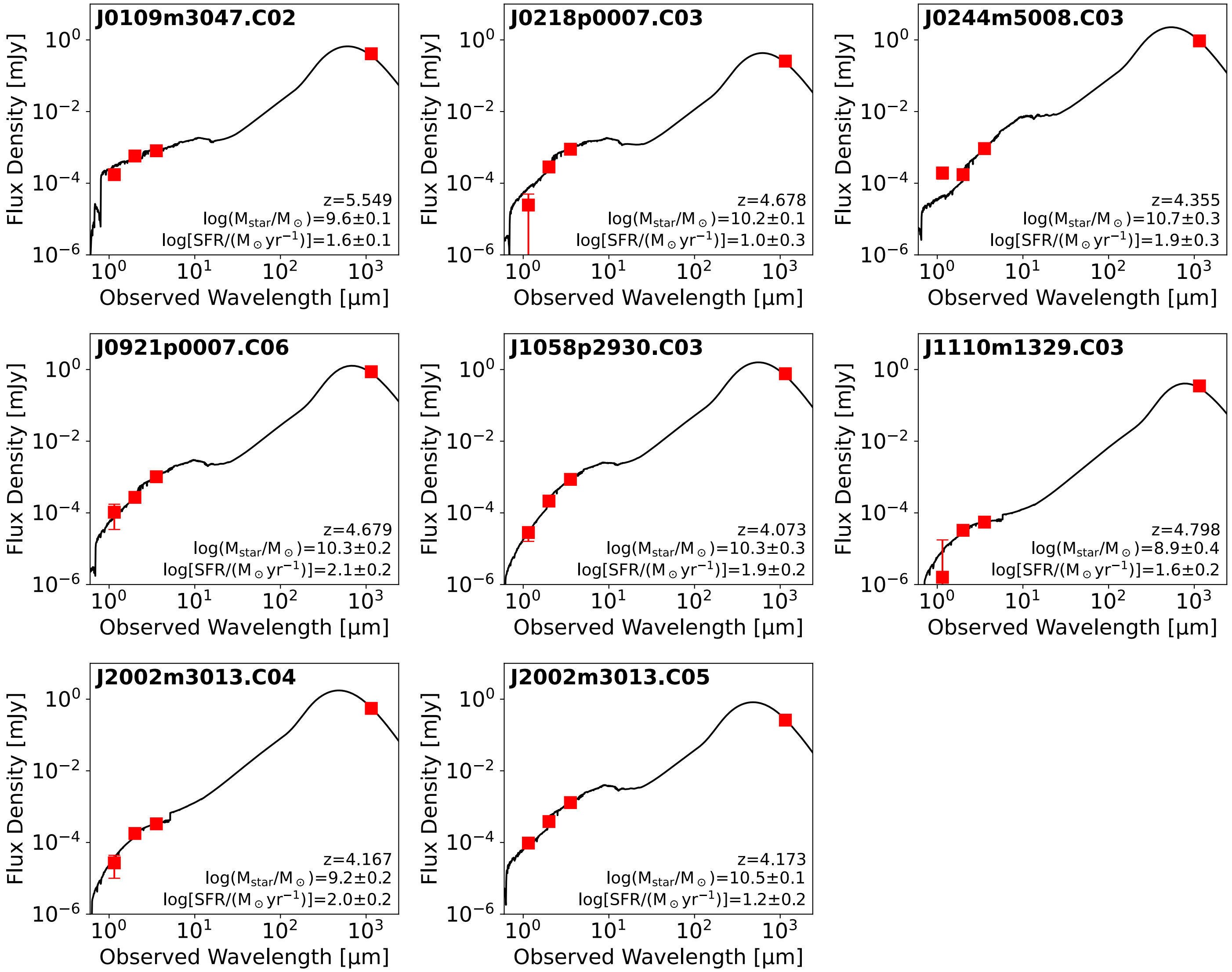

Figure 5. JWST and ALMA SEDs of eight DSFGs in ASPIRE sample. Photometric measurements are shown as red squares. Best-fit SED models obtained with CIGALE are shown as solid black curves. Source IDs, redshifts, derived stellar masses, and SFRs are indicated in the plots.

Table 2
Physical Properties of ASPIRE DSFGs at $z = 4$–6 Derived from SED Modeling

ID	$\log[M_{\rm star}/M_\odot]$	$\log[{\rm SFR}_{10\,{\rm Myr}}/(M_\odot\ {\rm yr}^{-1})]$	$\log[{\rm SFR}_{\rm UV}/(M_\odot\ {\rm yr}^{-1})]$	$\log[L_{\rm IR}/L_\odot]$	A_V/mag
J0109m3047.C02	9.6 ± 0.1	1.6 ± 0.1	0.9 ± 0.1	11.5 ± 0.1	0.6 ± 0.1
J0218p0007.C03	10.2 ± 0.1	1.0 ± 0.3	<0.4	11.4 ± 0.1	0.9 ± 0.2
J0244m5008.C03	10.7 ± 0.3	1.9 ± 0.3	0.8 ± 0.1	12.1 ± 0.2	2.4 ± 0.4
J0921p0007.C06	10.3 ± 0.2	2.1 ± 0.2	<0.9	12.0 ± 0.1	1.5 ± 0.3
J1058p2930.C03	10.3 ± 0.3	1.9 ± 0.2	−0.1 ± 0.2	11.9 ± 0.1	2.0 ± 0.3
J1110m1329.C03	8.9 ± 0.4	1.6 ± 0.2	<0.2	11.4 ± 0.2	2.1 ± 0.5
J2002m3013.C04	9.2 ± 0.2	2.0 ± 0.2	<0.2	11.8 ± 0.2	1.5 ± 0.2
J2002m3013.C05	10.5 ± 0.1	1.2 ± 0.2	0.4 ± 0.1	11.6 ± 0.1	1.4 ± 0.3

Notes. Light-weighted differential lensing magnification has been corrected for J0109m3047.C02 (see details in Appendix A). ${\rm SFR}_{10\,{\rm Myr}}$ is the SFR averaged over the last 10 Myr of SFH, which is slightly different from the dust-obscured ${\rm SFR}_{\rm IR}$ (based on $L_{\rm IR}$) that we use to infer the obscured SFRD (Section 4.4).

4. Results

4.1. Obscured Fraction of UV and Hα Star Formation

Most star formation in our ASPIRE DSFG sample at $z = 4$–6 is obscured by dust. If we define the obscured fraction of SFR as $f_{\rm obscured} = {\rm SFR}_{\rm IR}/({\rm SFR}_{\rm IR} + {\rm SFR}_{\rm UV})$ (e.g., K. E. Whitaker et al. 2017; Y. Fudamoto et al. 2020), then 96% ± 2% of their star formation is obscured by dust. Such an obscured fraction of SFR is significantly higher than the ALPINE sample of $M_{\rm star}$-selected galaxies with comparable mass and redshifts ($f_{\rm obscured} = 67^{+5}_{-7}\%$; Y. Fudamoto et al. 2020), suggesting that these ASPIRE DSFGs represent the dusty tail of the

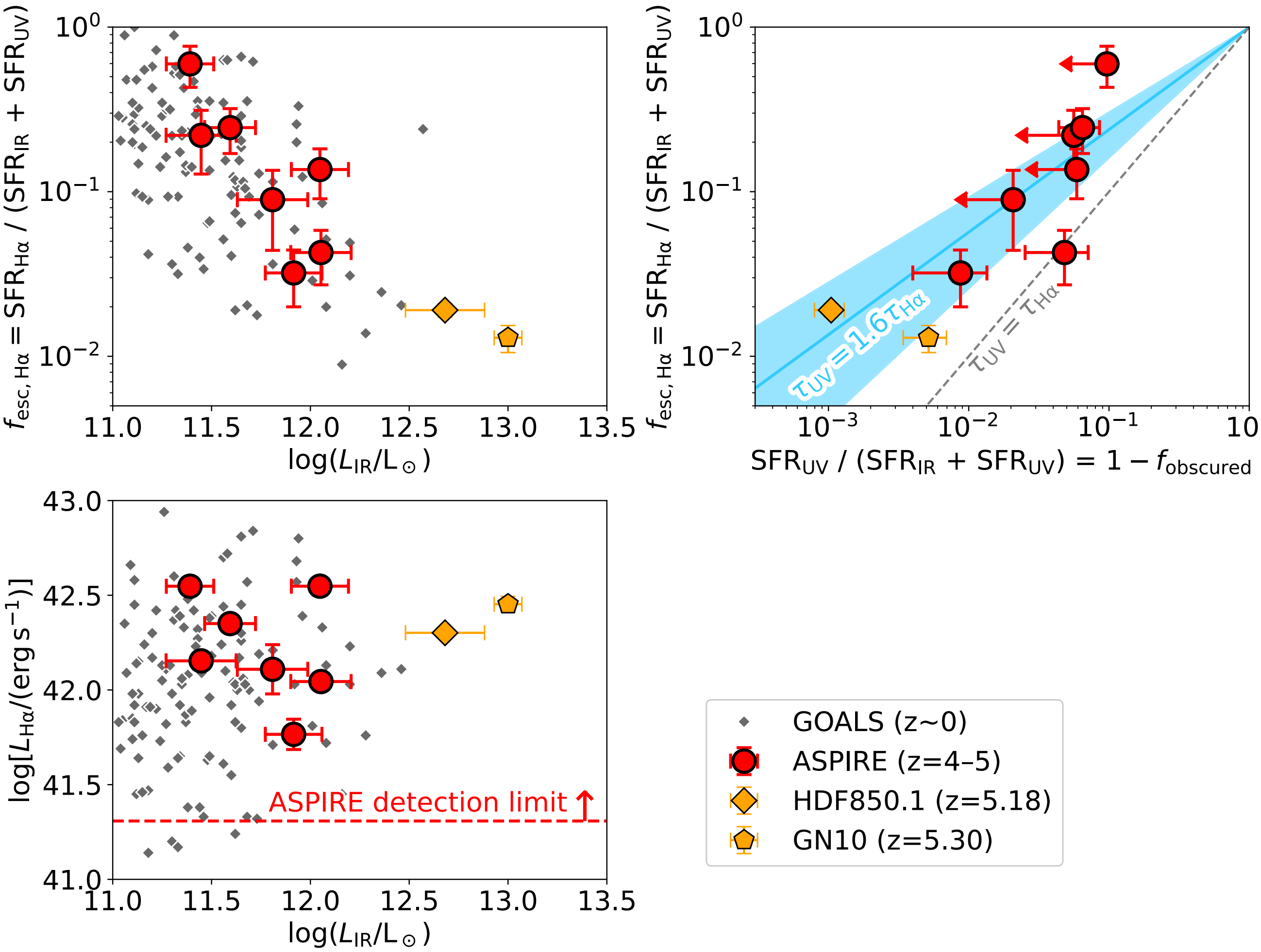

Figure 6. The dust obscuration and escape of Hα photons from DSFGs. In the top left panel, we show the escape fraction of Hα photons vs. IR luminosity. ASPIRE DSFGs are shown in red circles, and two $z > 5$ DSFGs in the FRESCO GOODS-N field (HDF850.1, GN10; measurements from F. Sun et al. 2024) are shown in orange symbols. Local (U)LIRGs in the GOALS sample are shown as small gray diamonds (L. Armus et al. 2009; J.-J. Jin et al. 2019). DSFGs with higher $L_{\rm IR}$ exhibit smaller escape fractions of Hα photons, resulting in a nearly constant Hα luminosity, i.e., $\log[L_{\rm H\alpha}/({\rm erg\ s^{-1}})] \simeq 42.0 - 42.5$, across a $\sim$ 2 dex wide span of $L_{\rm IR}$ as shown in the bottom left panel. In the top right panel, we plot the escape fraction of Hα vs. the escape fraction of UV ($1 - f_{\rm obscured}$). The dashed gray line indicates the scenario that the optical depths at UV ($\tau_{\rm UV}$; $\sim$ 2000 Å) and Hα ($\tau_{\rm H\alpha}$) wavelength are identical. The solid blue line and shaded region indicate the best-fit scaling relation and uncertainty $\tau_{\rm UV} = (1.61 \pm 0.34)\,\tau_{\rm H\alpha}$.

distribution of a wider star-forming galaxy population at this epoch. The obscured fractions of SFR for ASPIRE DSFGs are still slightly less than that of the most extreme DSFG at $z \sim 5$, e.g., HDF850.1 at $z = 5.18$ (D. H. Hughes et al. 1998; F. Walter et al. 2012), whose obscured fraction is $f_{\rm obscured} \sim 99.9\%$ (M. Xiao et al. 2024; F. Sun et al. 2024; see also T. Herard-Demanche et al. 2025). We also notice that D. T. Zimmerman et al. (2024) suggest an increase of $f_{\rm obscured}$ at fixed stellar mass at higher redshifts in the SIMBA cosmological simulations.

Among the ASPIRE DSFG sample at $z = 4$–6, five galaxies are undetected in the F115W band (rest-frame $\sim$2000 Å), and therefore they could be classified as HST-dark galaxies as introduced in Section 1. However, this is only a subset of 14 HST-dark galaxies selected with ALMA continuum detection and F115W nondetection ($<3\sigma$) among the full ASPIRE DSFG sample across all redshifts. This suggests a complex and broad redshift distribution of HST-dark galaxies, and the photometric redshifts obtained in optical and near-IR can be strongly degenerate with the dust attenuation and stellar age of the galaxies (e.g., J. S. Huang et al. 2011; K. I. Caputi et al. 2012; T. Wang et al. 2016). Fortunately, the successful detections of Hα and [O III] lines of these highly obscured DSFGs through NIRCam WFSS provide the critical redshift confirmation, allowing us to study the dust attenuation in these DSFGs with much higher accuracy than sources without $z_{\rm spec}$.

The top left panel of Figure 6 shows the escape fraction of Hα photons (defined as $f_{\rm esc,H\alpha} = {\rm SFR}_{\rm H\alpha}/({\rm SFR}_{\rm UV} + {\rm SFR}_{\rm IR})$; not to be confused with the escape fraction in a reionization/IGM context) versus $L_{\rm IR}$. Assuming a constant SFH, $f_{\rm esc,H\alpha}$ is mainly controlled by the dust extinction (although we caution that, compared to IR luminosity, Hα luminosity is less sensitive to star formation at $\gtrsim 10$ Myr; see the recent study of a $z = 2.4$ post-starburst DSFG by O. R. Cooper et al. 2024). It is clear that $f_{\rm esc,H\alpha}$ is strongly anticorrelated with $L_{\rm IR}$, both at $z \sim 5$ or in the local Universe (as seen with the LIRGs/ULIRGs in the GOALS sample; L. Armus et al. 2009, J.-J. Jin et al. 2019). Such an anticorrelation indicates that a larger fraction of Hα photons are dust-obscured in DSFG with more vigorous star formation activity. This is mainly driven by the fact that the Hα luminosity of $z \sim 5$ DSFG does not correlate with $L_{\rm IR}$ (Spearman's $\rho = -0.05$, p-value = 0.9), because of complex dust–stellar geometry (e.g., M. Garcìa-Marìn et al. 2009; C. Giménez-Arteaga et al. 2022). As shown in the bottom left panel of Figure 6, the Hα luminosity of $z \sim 5$ DSFG remains almost constant (i.e., $\log[L_{\mathrm{H}\alpha}/(\mathrm{erg\ s}^{-1})] \simeq 42.0-42.5$) across an almost 2 dex wide span of L_{IR}. Such a characteristic Hα luminosity range is well above the 5σ detection limit of ASPIRE (and also FRESCO; P. A. Oesch et al. 2023). Also as shown in the same plot, if local (U)LIRGs were placed at $z \sim 5$, then 96% of them would be above our ASPIRE Hα luminosity detection threshold. Therefore, we conclude that the NIRCam grism spectroscopic surveys of high-redshift DSFGs are highly efficient and complete.

The escape fraction of UV photons (defined as $f_{\mathrm{esc,UV}} = 1 - f_{\mathrm{obscured}} = \mathrm{SFR}_{\mathrm{UV}}/(\mathrm{SFR}_{\mathrm{IR}} + \mathrm{SFR}_{\mathrm{UV}})$) is also controlled by dust extinction under the stable SFH assumption. A tight correlation between $f_{\mathrm{esc,UV}}$ and $f_{\mathrm{esc,H}\alpha}$ can demonstrate that these escape fractions are mostly driven by the dust obscuration instead of complex SFH because UV, Hα, and far-IR emissions are sensitive to SFH at different timescales. Therefore, we compare the escape fractions of Hα and UV photons in the top right panel of Figure 6. Both the UV and Hα escape fractions are controlled by the optical depth at their wavelengths, i.e., $f_{\mathrm{esc,UV}} = \exp(-\tau_{\mathrm{UV}})$ and $f_{\mathrm{esc,H}\alpha} = \exp(-\tau_{\mathrm{H}\alpha})$. We find that the typical $\tau_{\mathrm{UV}}/\tau_{\mathrm{H}\alpha}$ ratio of $z \sim 5$ DSFGs is 1.61 ± 0.34.

Under the D. Calzetti et al. (2000) extinction curve with negligible 2175 Å bump, the dust optical depth ratio between UV (~ 2000 Å) and Hα wavelength is ~ 2.7. This is larger than the ratio derived above, because nebular emission lines originate from stellar birth clouds with stronger dust attenuation, and in certain cases Hα from IR-luminous regions could be totally obscured (e.g., M. Pereira-Santaella et al. 2015; L. Colina et al. 2023; A. Bik et al. 2024; F. Sun et al. 2024; H. Übler et al. 2024). Therefore, the reduction factor to be applied on the nebular gas emission line $E(B-V)_g$ to derive stellar continuum $E(B-V)_s$ is 0.60 ± 0.13 for $z \sim 5$ DSFGs, which is slightly higher than the canonical factor of 0.44 ± 0.03 with a D. Calzetti et al. (2000) extinction curve (D. Calzetti 1997). A larger reduction factor suggests that the difference of dust geometry between UV and nebular emission is smaller for $z \sim 5$ DSFGs when compared to local starburst galaxies. This also increases the detectability of Hα emission of DSFGs at high redshifts. However, we also notice that the reduction factor is sensitive to the slope of underlying extinction curve. If the underlying extinction curve of high-redshift DSFGs is steeper, i.e., following the SMC curve (K. D. Gordon et al. 2003), then the reduction factor could be smaller (0.38 ± 0.08).

4.2. Number Count of DSFGs at $z = 4$–6

One key focus of this study is to understand the number density of DSFGs at $z = 4$–6 and their contribution to the IRLF and SFRD. To measure these quantities, we first compute the effective survey area above our detection limits in the native and tapered ALMA mosaics. We make use of the rms noises of these mosaics and the primary beam response maps to compute the effective survey area above each flux density limits, i.e., $A_{\max}(S_{1.2\,\mathrm{mm}})$. Given the brightness of galaxies in our sample (observed $S_{1.2\,\mathrm{mm}} \geqslant 0.28$ mJy; much larger than the ~ 0.15 mJy detection limit), these sources can be selected in most of our survey footprint ($A_{\max}$ ranges from 24 to 35 arcmin^2 for each source). Note that, for the lensed source J0109m3047.C02, the $A_{\max}$ is computed using the lensing-corrected 1.2 mm flux density ($S_{1.2\,\mathrm{mm}} = 0.24$ mJy).

By simply summing the $1/A_{\max}$ of ASPIRE DSFGs and correcting for the redshift desert at $z \simeq 5.0$–5.3 where Hα or [O III] cannot be detected with NIRCam WFSS survey with the F356W filter, we find a surface density of $\sim 1.1 \times 10^3\ \mathrm{deg}^{-2}$ for $z = 4$–6 DSFGs at $S_{1.2\,\mathrm{mm}} \geqslant 0.24$ mJy. This is roughly twice the surface density of the HST H-dropout galaxies at $z \simeq 3-6$ and $S_{0.87\,\mathrm{mm}} \geqslant 0.6$ mJy (~ 530 deg^{-2}; T. Wang et al. 2019). The survey depth in terms of L_{IR} is very similar for ASPIRE and the ALMA follow-up studies in T. Wang et al. (2019). Although the conventional H-dropout selection with HST and Spitzer/IRAC has identified obscured star formation that was previously missed by rest-frame UV surveys, such a selection will also miss (i) $z > 4$ DSFGs that are not totally obscured at HST wavelengths (J–H band), e.g., because of patchy dust geometry, and (ii) highly dust-attenuated objects that are faint at 3–5 μm and below the Spitzer/IRAC detection limit.

We measure the differential number count (dN/dS) of ASPIRE DSFGs at $z = 4$–6 through the $1/A_{\max}$ method:

$$\frac{dN}{dS} = \frac{1}{d\log S}\sum_i \frac{1}{C_i A_{\max}(S_i)}, \quad (1)$$

where $d\log S$ is the flux density bin size in log scale, C_i is the completeness for the ith source in the bin, and $A_{\max}(S_i)$ is the effective survey area above the source flux density S_i.

We present the completeness correction simulation in Appendix B, and as a quick summary, our ALMA continuum source selection is highly complete (>95% for all sources) because of the high fidelity of detections (S/N $\geqslant$ 6.5). Strictly speaking, because of multiple redshift gaps with NIRCam WFSS survey in the F356W band (Section 3.1), the full ASPIRE DSFG sample is not spectroscopically complete across all redshifts. However, we argue that we have reached a high spectroscopic completeness at $z = 4-5$ and 5.3–6 because the Hα and [O III] luminosities of sources in our sample are well above the 5σ detection limit (indicated by the dashed red line in lower left panel of Figure 6). Even if the completeness of [O III] spectroscopy for DSFGs cannot be properly assessed because of the limited JWST data obtained so far (high-redshift DSFGs may exhibit a diverse distribution of [O III] strengths; e.g., J. McKinney et al. 2023a; L. Barrufet et al. 2025; F. Sun et al. 2024), we argue that the number density of DSFGs at $z > 5$ should be naturally smaller than that at $z < 5$, just as we observed. Therefore, the true number density of DSFGs at $z = 4$–6 should be close to our measurement, or only slightly higher.

We set two flux density bins at 0.15–0.47 and 0.47–1.5 mJy (bin size is 0.5 dex). We also run a Monte Carlo (MC) simulation to draw 1.2 mm flux density from the observed values and errors, compute the corresponding $A_{\max}$ and completeness, and then derive the number count and its uncertainty. The uncertainty includes Poisson error following the prescription of N. Gehrels (1986), and we also include the error from cosmic variance (shot noise) following the prescription of B. P. Moster et al. (2011) (the same method as that adopted by J. McKinney et al. (2024) for DSFGs in the COSMOS-web field), which is computed using the geometry of survey footprint (25 fields with area of $1\overset{\prime}{.}2 \times 1\overset{\prime}{.}2$), redshift interval ($\Delta z = 1.7$ around $z = 5$), dark matter correlation function, and the σ_8 and galaxy bias at $z \sim 5$ (0.17 and ~ 8). The uncertainty from cosmic variance (~0.05 dex) is much smaller than that from Poisson error (~ 0.28 dex in each bin), and we also experiment with other cosmic variance

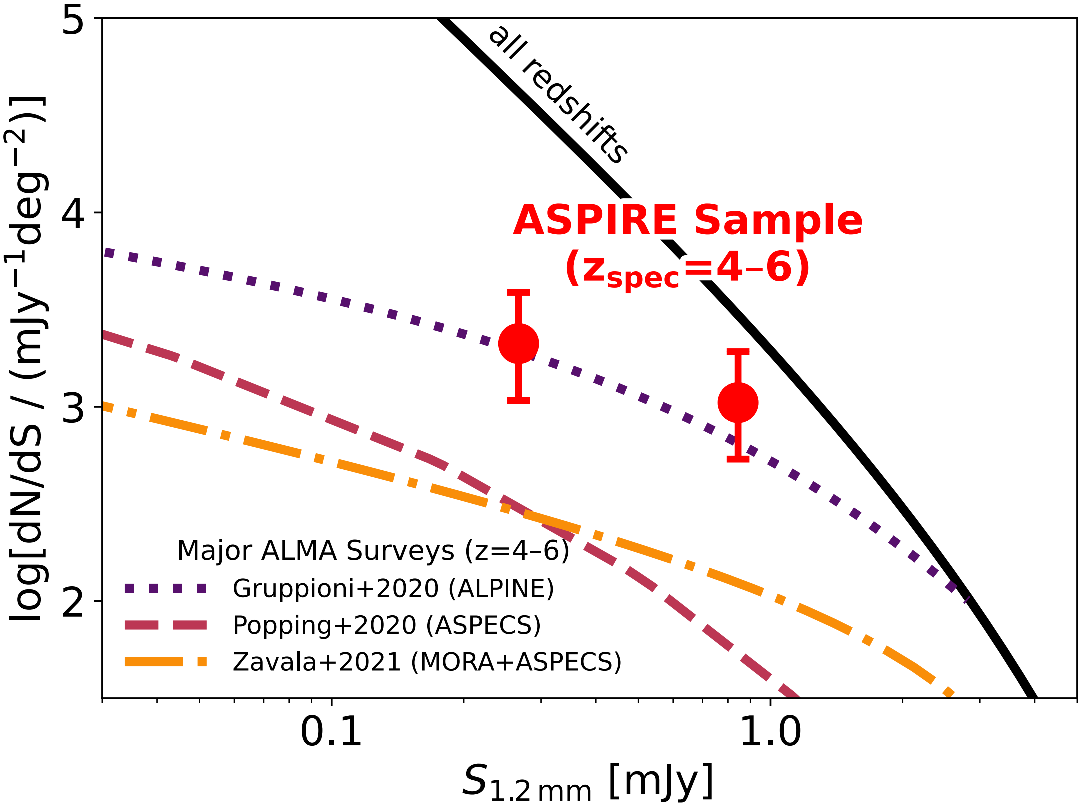

Figure 7. Differential 1.2 mm number count of DSFGs at $z = 4–6$ measured with the ASPIRE sample (solid red circles). For comparison, we show the 1.2 mm number count of DSFGs at all redshifts (S. Fujimoto et al. 2023; solid black line), and the number count of DSFGs at $z = 4–6$ estimated based on the works of C. Gruppioni et al. (2020; based on the ALPINE survey; dotted purple line) and J. A. Zavala et al. (2021; based on the MORA and ASPECS surveys; dashed–dotted orange line) assuming their best-fit IRLFs and galaxy SEDs, and the semi-empirical model from G. Popping et al. (2020; based on the ASPECS survey; dashed maroon line).

prescriptions and find similar results (0.05–0.07 dex; M. Trenti & M. Stiavelli 2008; S. P. Driver & A. S. G. Robotham 2010).

Figure 7 shows the 1.2 mm number of DSFGs at $z = 4–6$ measured from the ASPIRE survey (red circles). We highlight the fact that the only noticeable uncertainty of our measurement is from Poisson statistics, not cosmic variance or any other astrophysical assumption (e.g., $z_{\rm phot}$ or SED model). The number count of $z = 4–6$ DSFGs seems to be much flatter than the 1.2 mm number count of DSFGs across all redshifts (solid black line, S. Fujimoto et al. 2023; see also S. Fujimoto et al. 2016; J. González-López et al. 2020; C. Gómez-Guijarro et al. 2022; J. Chen et al. 2023; S. Adscheid et al. 2024, which cover similar $S_{1.2\,\rm mm}$ spaces). This indicates a larger fraction of DSFGs at higher redshifts toward the bright end of millimeter number count function (e.g., M. Béthermin et al. 2017; C. M. Casey et al. 2018b, 2021; C. d. P. Lagos et al. 2020; C.-C. Chen et al. 2022; F. Sun et al. 2022).

For comparison, we also show the number count of DSFGs at $z = 4–6$ based on the semi-empirical model from G. Popping et al. (2020; based on the ASPECS survey) and IRLFs modeled by C. Gruppioni et al. (2020; based on the ALPINE survey) and J. A. Zavala et al. (2021; based on the MORA and ASPECS surveys). To convert IRLFs in the literature to number counts, we assume far-IR SEDs similar to those assumed in these original works. In J. A. Zavala et al. (2021), the authors derived a best-fit dust emissivity $\beta_{\rm em} \sim 1.8$ from their backward modeling, and they assumed a relation between the rest-frame wavelength of the far-IR SED peak and IR luminosity ($\lambda_{\rm peak} - L_{\rm IR}$; C. M. Casey et al. 2018b), which corresponds to a modified blackbody (MBB) $T_{\rm dust} \sim 32$ K at $L_{\rm IR} = 10^{12} L_{\odot}$ through C. M. Casey (2012) parameterization. In C. Gruppioni et al. (2020), the authors made use of the best-fit far-IR SED through multiple templates included in the software LE PHARE (S. Arnouts & O. Ilbert 2011). Therefore, we convert their best-fit IRLF at $z = 3.5-6$ to a 1.2 mm number count assuming the R. Chary & D. Elbaz (2001) far-IR SED templates, one of the major template sets adopted by LE PHARE (effectively $T_{\rm dust} \sim 45$ K and $\beta_{\rm em} \sim 1.5$ for $S_{1.2\,\rm mm} \sim 0.5$ mJy sources at $z \sim 5$).

The number count of $z = 4–6$ DSFGs from the ASPIRE sample is similar to that of C. Gruppioni et al. (2020) based on nontarget ALMA Band-7 continuum galaxies discovered through the ALPINE survey (M. Béthermin et al. 2020; O. Le Fèvre et al. 2020). Because the primary targets of the ALPINE survey are star-forming galaxies at $z \sim 5$, it has been speculated that the excess of the $z = 4–6$ DSFG number count from ALPINE (relative to ASPECS) may arise from the clustering of nontarget DSFGs around their main targets (e.g., J. A. Zavala et al. 2021). Our observations suggest that the number density of $z = 4–6$ DSFGs measured from the ALPINE survey is sufficiently accurate despite uncertainties with $z_{\rm phot}$.

Our measurements are higher than the models based on ASPECS survey (G. Popping et al. 2020; J. A. Zavala et al. 2021) by $\sim$ 1 dex. Such a large discrepancy cannot be explained by any form of error from the ASPIRE sample. We think the large difference is caused by the strong shot noise with the ASPECS sample ($\sigma \sim 0.5$ dex, including both Poisson error and cosmic variance). M. Aravena et al. (2020) showed that no DSFG at $z > 4$ was blindly discovered with the ASPECS deep 1 mm or 3 mm survey. In contrast, the eight DSFGs in our sample are discovered along 7 out of 25 quasar sightlines, and therefore the chance to detect one DSFG at $z = 4$–6 within the 1.4 arcmin^2 survey area per sightline is only 28%. The survey area of ASPECS in the HUDF is $\sim$ 3 times that of a typical ASPIRE field/sightline, and thus the chance to detect zero DSFG at $z = 4$–6 is $(1-28\%)^3 \sim 37\%$, a non-negligible probability. Therefore, we attribute the discrepancy between ASPIRE and ASPECS measurements to the under-density of $z = 4$–6 DSFGs in the HUDF region. Similar conclusions have been drawn from previous studies for DSFGs (e.g., S. Fujimoto et al. 2023) and even for Lyman-break galaxies and AGN (e.g., L. L. Cowie et al. 2002; A. Moretti et al. 2003; F. E. Bauer et al. 2004; P. A. Oesch et al. 2007).

4.3. Spectroscopically Complete Infrared Luminosity Function

We further measure the IRLF at $z = 4$–6 from the ASPIRE DSFG sample. Such an IRLF is spectroscopically complete down to $L_{\rm IR} \sim 2 \times 10^{11}\,L_\odot$ and almost free from the impact of cosmic variance. Similar to the method presented in Section 4.2, we adopt the $1/V_{\rm max}$ method (M. Schmidt 1968):

$$\Phi(L) = \frac{1}{d\log L}\sum_i \frac{1}{C_i V_{\rm max}(L_i)}, \tag{2}$$

where $d\log L$ is the luminosity bin size in log scale, C_i is the completeness for the ith source in the bin, and $V_{\rm max}(L_i)$ is the effective survey volume above the source luminosity L_i. We make use of $L_{\rm IR}$ and uncertainties measured from CIGALE energy-balance SED fitting. The uncertainty of $L_{\rm IR}$ and IRLF propagated from loosely constrained $T_{\rm dust}$ is further discussed in Section 5.1.

We set three $L_{\rm IR}$ bins at $10^{11.2}$–$10^{11.6}$, $10^{11.6}$–$10^{12.0}$, and $10^{12.0}$–$10^{12.4}\,L_\odot$. Similarly to Section 4.2, we also run MC simulation to randomly draw $L_{\rm IR}$ from the SED-derived $L_{\rm IR}$ and uncertainties. The ratio of drawn $L_{\rm IR}$ and best-fit $L_{\rm IR}$ is applied to scale the ALMA S/N for the completeness and effective survey volume calculation. The uncertainty of our luminosity function measurements includes the standard deviation from MC simulation, Poisson error (following N. Gehrels 1986), and cosmic variance ($\sim$ 0.05 dex, negligible; following the prescription of B. P. Moster et al. 2011), respectively. The derived IRLF is presented in Table 3 and Figure 8.

At the $L_{\rm IR}$ range probed by ASPIRE DSFGs, the availability of measurements in literature is limited. This is because these DSFGs are typically below the detection limit of single-dish telescope at (sub)millimeter wavelengths (e.g., JCMT/SCUBA2 and Herschel/SPIRE). Our measurements are consistent with those of S. Fujimoto et al. (2023) based on ALCS data in lensing cluster fields, and also broadly consistent with the measurements from C. Gruppioni et al. (2020) and A. Traina et al. (2024) in their lowest-luminosity bins. Nevertheless, we observe a flattening of IRLF toward the faint end, and the volume density of LIRGs at $z = 4$–6 is somewhat lower than many model predictions (e.g., C. d. P. Lagos et al. 2020; J. W. Trayford et al. 2020; M. Béthermin et al. 2022; A. P. Vijayan et al. 2022).

We fit the measured IRLF with a double-power-law model following S. Fujimoto et al. (2023):

$$\Phi(L) = \Phi^\star\left[\left(\frac{L}{L^\star}\right)^\alpha + \left(\frac{L}{L^\star}\right)^\beta\right]^{-1}, \tag{3}$$

Table 3
Infrared Luminosity Function at $z = 4$–6 Measured with ASPIRE DSFGs

Observed Infrared Luminosity Function			
$\log(L_{\rm IR}/L_\odot)$	11.2–11.6	11.6–12.0	12.0–12.4
$< N >$	2.71	2.88	1.63
$\log[\Phi/({\rm Mpc^{-3}dex^{-1}})]$	$-4.04^{+0.35}_{-0.39}$	$-4.27^{+0.35}_{-0.39}$	$-4.51^{+0.42}_{-0.50}$
Best-fit Double-power-law Parameters			
$\log[\Phi^\star/({\rm Mpc^{-3}dex^{-1}})]$	$\log(L^\star_{\rm IR}/L_\odot)$	α	β
$-4.52^{+0.49}_{-0.55}$	$12.58^{+0.26}_{-0.29}$	$0.59^{+0.39}_{-0.45}$	$3.24^{+1.63}_{-0.95}$

Notes. $\log(L_{\rm IR}/L_\odot)$ is the luminosity bin, $< N >$ is the average number of sources in the luminosity bin through MC simulations, and $\log[\Phi/({\rm Mpc^{-3}dex^{-1}})]$ is the measured volume density of sources in the luminosity bin. Parameters for the IRLF are derived assuming a double-power-law function through EMCEE (Section 4.3).

where $L^\star$ and $\Phi^\star$ are the characteristic luminosity and volume density, respectively. We define α and β as the faint-end and bright-end slopes of LF, respectively. We obtain a Monte Carlo Markov Chain (MCMC) fitting of the function above using EMCEE (D. Foreman-Mackey et al. 2013). Because ASPIRE data do not constrain the bright end of IRLF toward $\sim 10^{13}\,L_\odot$, we have to include literature measurements from M. P. Koprowski et al. (2017), C. Gruppioni et al. (2020), S. Fujimoto et al. (2023), and A. Traina et al. (2024) into our fitting. All literature samples included here are not spectroscopically complete. Therefore, we artificially increase their uncertainties by a factor of $\sqrt{2}$ to reduce their weighting in the fitting and compensate for potentially underestimated errors from $z_{\rm phot}$. The allowed ranges for the double-power-law parameters are $-10 < \log(\Phi^\star) < 0$, $11 < \log(L^\star) < 14$, $-0.5 < \alpha < 1.5$, and $1.5 < \beta < 7.0$. All prior distributions are flat.

The best-fit IRLF and its uncertainties (16–84th percentile) are indicated with the solid red line and shaded region in Figure 8, respectively. The best-fit parameters of IRLF and uncertainties are also presented in Table 3. We find that the combined ASPIRE and ALCS measurements yield a flattened faint-end slope of $\alpha = 0.59^{+0.39}_{-0.45}$, in between the faint-end slope measured by J. A. Zavala et al. (2021; $\sim$ 0.4) and that of S. Fujimoto et al. (2023; $\sim$ 0.9). Although large uncertainties are seen with all of these parameters, as shown in the corner plot of our MCMC fitting (Figure 9), $\log(\Phi^\star)$, α and β are all strongly degenerate with $\log(L^\star)$. Therefore, the integral of the IRLF (i.e., obscured SFRD) can be measured relatively accurately (Section 4.4). Future spectroscopic constraints of $z = 4$–6 IRLF at $L_{\rm IR} \gtrsim L^\star$ will be very helpful to accurately determine $L^\star$ and other parameters (Section 5.2).

4.4. Obscured Star Formation Rate Density

We compute the obscured cosmic SFRD using the derived IRLF. Similarly to S. Fujimoto et al. (2023), we integrate the IRLF down to $L_{\rm IR} = 10^{10}\,L_\odot$, which corresponds to $\sim 0.0025L^\star$. Because of the flattening of the IRLF toward the faint end, the integral of the IRLF down to $L_{\rm IR} = 10^{9}\,L_\odot$ is only higher than that down to $L_{\rm IR} = 10^{10}\,L_\odot$ by $\sim$ 0.03 dex. We convert the integral of the IRLF to an obscured SFRD using the factor listed in Section 3.2. We derive an obscured SFRD of $\log[\rho_{\rm SFR,IR}/(M_\odot\,{\rm yr^{-1}Mpc^{-3}})] = -1.52^{+0.14}_{-0.13}$ at $z = 4$–6 (median $z = 4.5$).

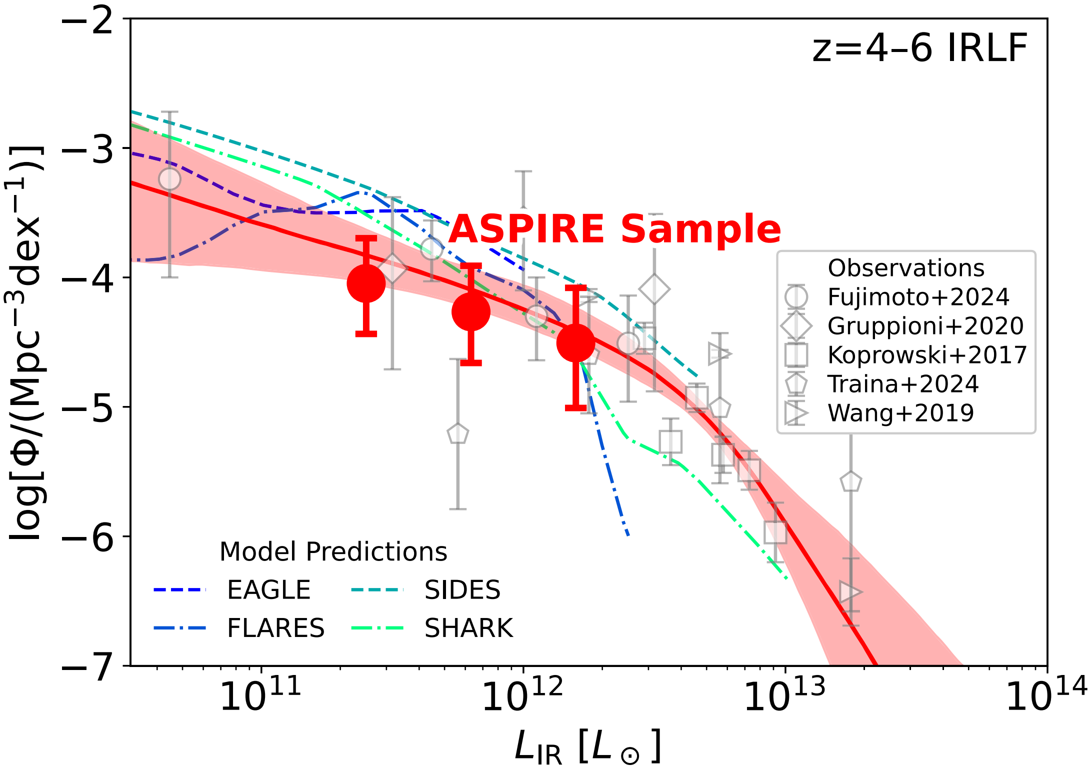

Figure 8. Spectroscopically complete infrared luminosity function at $z = 4–6$ measured with the ASPIRE sample (solid red circles). The best-fit IRLF and its uncertainties (16–84th percentile) are indicated with the solid red line and shaded region, respectively. For comparison, we use open gray symbols to show the direct measurements from previous observations (incomplete with spectroscopy), which include those of M. P. Koprowski et al. (2017), L. Wang et al. (2019), C. Gruppioni et al. (2020), S. Fujimoto et al. (2023), and A. Traina et al. (2024). Colored lines show theoretical model predictions, which include those of EAGLE (J. W. Trayford et al. 2020), FLARES (A. P. Vijayan et al. 2022), SIDES (M. Béthermin et al. 2022), and SHARK (C. d. P. Lagos et al. 2020).

Figure 10 shows the obscured and unobscured SFRD measurements at $z \simeq 0-7$ in the literature, and the ASPIRE measurement is highlighted as the red diamond. At $z \gtrsim 4$, previous determinations of obscured SFRD are highly uncertain, with a wide dispersion over 1 dex span (e.g., M. Rowan-Robinson et al. 2016; J. S. Dunlop et al. 2017; M. P. Koprowski et al. 2017; D. Liu et al. 2018; C. Gruppioni et al. 2020; Y. Khusanova et al. 2021; J. A. Zavala et al. 2021; B. Magnelli et al. 2024; A. Traina et al. 2024). Our determination is within the dispersion of these previous measurements, and specifically, our measurement is about five times the obscured SFRD derived by J. A. Zavala et al. (2021) through a backward modeling of millimeter number counts. As mentioned in Section 4.2, we caution that the strong cosmic variance and the absence of $z > 4$ DSFGs in the HUDF region could affect the number counts at 1 and 3 mm used by J. A. Zavala et al. (2021). The uncertainty from the far-IR SED can also lead to errors in SFRD determination with both the backward modeling method (C. M. Casey et al. 2018b; J. A. Zavala et al. 2021) and also our direct determination, which will be further discussed in Section 5.1.

We also compare our measurement with the so-called "dust-poor" and "dust-rich" scenarios of obscured SFRD evolution proposed by C. M. Casey et al. (2018b). Our result is in between these two model predictions at $z \sim 4.5$. The ASPIRE-obscured SFRD is also comparable to the total SFRD (UV + IR) at $z \sim 4.5$ from the P. Madau & M. Dickinson (2014) best-fit model ($\log[\rho_{\rm SFR,total}/(M_\odot\ {\rm yr}^{-1}{\rm Mpc}^{-3})] = -1.60$). Similar conclusions have also been drawn by S. Fujimoto et al. (2023), based on recent ALCS observations suggesting that the total SFRD at $z = 4–6$ could have been underestimated previously.

To understand the total amount and obscured fraction of SFRD at $z = 4–6$, we compile the unobscured SFRD measurements from rest-frame UV surveys at $z = 0–7$ (N. A. Reddy & C. C. Steidel 2009; O. Cucciati et al. 2012; R. J. Bouwens et al. 2015; S. L. Finkelstein et al. 2015; A. Alavi et al. 2016; V. Mehta et al. 2017; R. Bouwens et al. 2020; T. Moutard et al. 2020; L. Sun et al. 2023). Following P. Madau & M. Dickinson (2014), we fit the redshift evolution of unobscured SFRD with the following function:

$$\rho_{\rm SFR,UV}(z) = \Psi_0 \frac{\left(\frac{1+z}{1+z_0}\right)^a}{\left[1+\left(\frac{1+z}{1+z_0}\right)^b\right]} M_\odot {\rm yr}^{-1}{\rm Mpc}^{-3}, \quad (4)$$

and we derive $z_0 = 3.74 \pm 0.27$, $\log(\Psi_0) = -1.37 \pm 0.03$, $a = 1.57 \pm 0.16$, and $b = 5.85 \pm 0.33$. This implies an unobscured SFRD of $\log[\rho_{\rm SFR,UV}/(M_\odot.{\rm yr}^{-1}{\rm Mpc}^{-3})] = -1.80$ at $z \sim 4.5$, which is about half of the obscured SFRD that we derived based on ASPIRE data. Therefore, we conclude that $66^{+7}_{-7}\%$ of the total SFRD is obscured by dust at this epoch. The total SFRD that we derive is $\log[\rho_{\rm SFR,total}/(M_\odot\ {\rm yr}^{-1}{\rm Mpc}^{-3})] = -1.34^{+0.10}_{-0.08}$, which is $180^{+46}_{-30}\%$ of the total SFRD from P. Madau & M. Dickinson (2014) best-fit model (similar to the conclusion in S. Fujimoto et al. 2023).

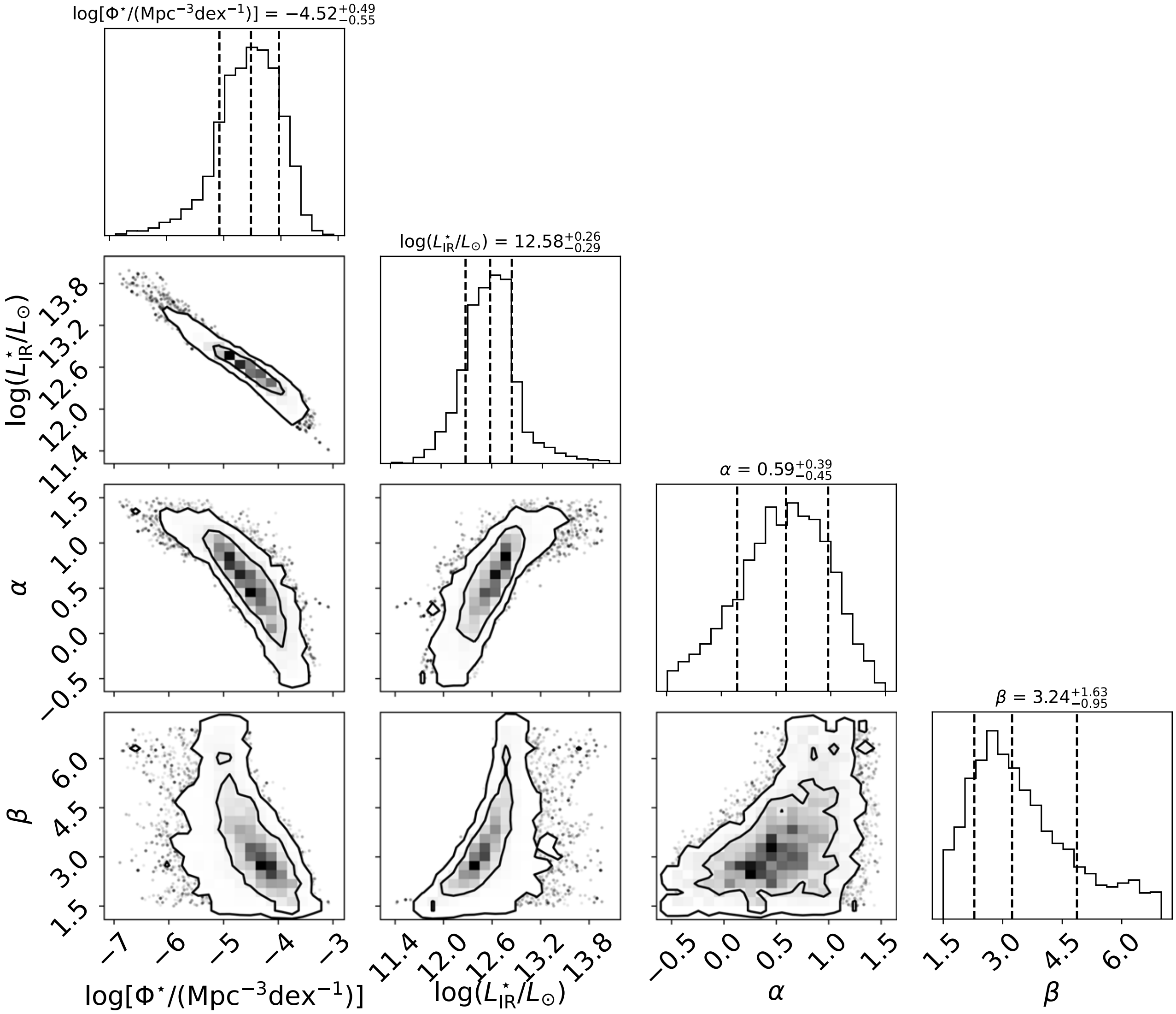

Figure 9. MCMC corner plot of the double-power-law parameters for the IRLF fitting (Figure 8 and Section 4.3). Contours are at $1-2\sigma$.

5. Discussion

In this section, we discuss the potential caveats of our determinations of the IRLF and SFRD. We also propose improvements that could be made through observations in the near future.

5.1. Far-IR SED

In order to determine IRLF and SFRD, we make use of the energy-balance SED fitting code CIGALE to derive L_{IR} (Section 3.2). The accuracy of L_{IR} thus relies on the validity of the energy-balance and far-IR SED assumptions.

It is known that DSFGs may not obey the energy-balance assumption along the observed sightline, simply because of patchy dust geometry. Previous studies have shown that DSFGs can have relatively blue UV continuum slopes, placing them above the IRX $-$ β_{UV} relation for normal star-forming galaxies (e.g., K. Penner et al. 2012; I. Oteo et al. 2013; C. M. Casey et al. 2014b). One of the most recent examples is HDF850.1 at $z = 5.18$, which is $\sim$ 100 times greater than the IRX $-$ β_{UV} relation because of the leakage of UV photons (F. Sun et al. 2024). A similar effect has been seen for at least one DSFG in the ASPIRE sample (J0244m5008.C03), and the best-fit SED model does not reproduce the flux density in the F115W band satisfactorily (Figure 5).

To quantify the potential uncertainty of obscured SFRD determination with the energy-balance assumption (hereafter the “benchmark” SFRD), we derive the IRLF and obscured SFRD following the same methods presented in Section 4 but assuming different dust temperatures.

First of all, the CIGALE best-fit L_{IR} used by “benchmark” SFRD is roughly equivalent to that computed from modified blackbody SED with T_{dust} = 33 K and β_{em} = 1.8. This is similar to the typical T_{dust} for galaxies with $L_{\mathrm{IR}} = 10^{12}\,L_\odot$ observed out to $z \sim 4.5$ (F. Sun et al. 2022; also modeled with MBB SED with β_{em} = 1.8), in which the direct T_{dust} measurements were obtained through Herschel/SPIRE at 250–500 μm thanks to lensing magnification.

However, arguably there is no consensus regarding the typical T_{dust} for LIRGs at $z \sim 5$. On one hand, studies have suggested that M_{star}-selected galaxies have higher dust temperatures at higher redshifts, based on the stacking of Herschel data (B. Magnelli et al. 2014; C. Schreiber et al. 2018), although caution should be taken due to the large beam

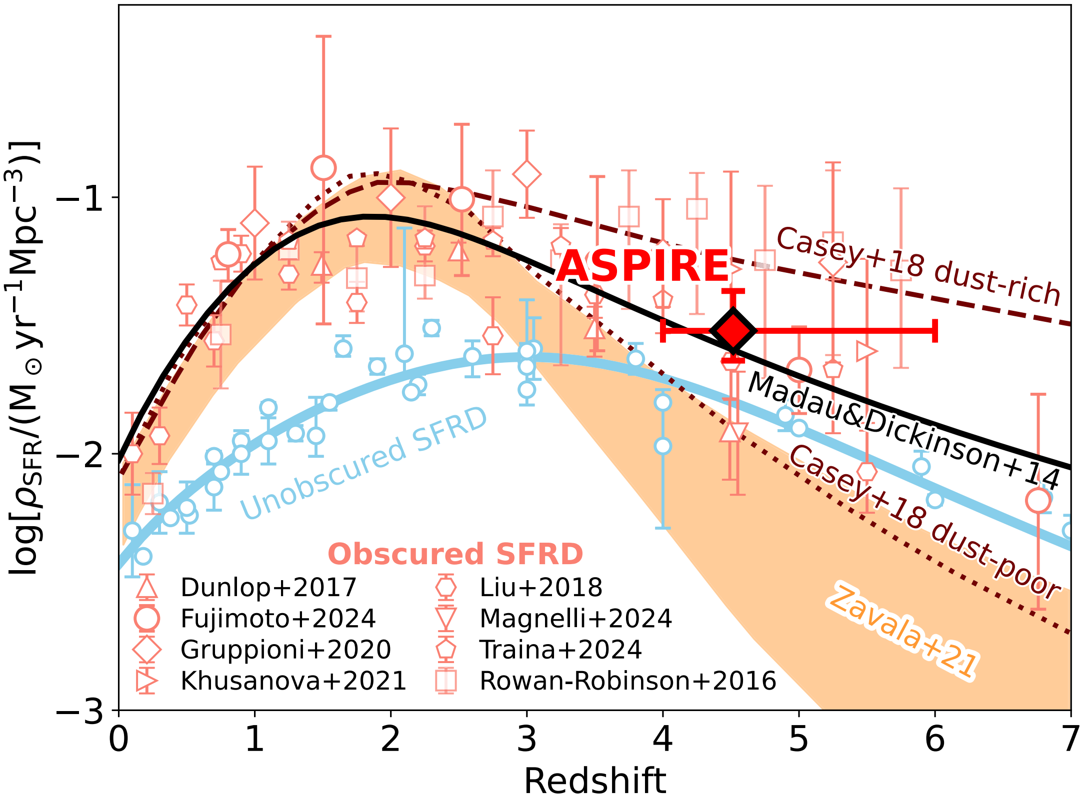

Figure 10. Obscured cosmic star formation rate density measured with the ASPIRE sample at $z = 4$–6 (red diamond). For comparison, we use open salmon-pink symbols to plot literature measurements of the obscured SFRD, including those of M. Rowan-Robinson et al. (2016), J. S. Dunlop et al. (2017), D. Liu et al. (2018), C. Gruppioni et al. (2020), Y. Khusanova et al. (2021), S. Fujimoto et al. (2023), B. Magnelli et al. (2024), and A. Traina et al. (2024). Unobscured SFRDs measured in rest-frame UV are shown as open sky-blue circles (N. A. Reddy & C. C. Steidel 2009; O. Cucciati et al. 2012; R. J. Bouwens et al. 2015; S. L. Finkelstein et al. 2015; A. Alavi et al. 2016; V. Mehta et al. 2017; R. Bouwens et al. 2020; T. Moutard et al. 2020; L. Sun et al. 2023), and the best-fit redshift-evolution model is indicated by the solid sky-blue curve. The C. M. Casey et al. (2018b) "dust-rich" and "dust-poor" scenarios are shown as dashed and dotted maroon lines, respectively. The inferred obscured SFRDs from a backward evolution model of 1–3 mm number counts (J. A. Zavala et al. 2021) are shown as an orange shaded region. The solid black line shows the best-fit total SFRD from P. Madau & M. Dickinson (2014). The G. Chabrier (2003) IMF has been assumed for all SFRD measurements in this plot.

size (up to $\sim 35''$). Having higher dust temperatures at higher redshifts is a natural consequence of warmer cosmic microwave background (CMB) heating. On the other hand, direct $T_{\rm dust}$ measurements of $L_{\rm IR}$-selected DSFGs also suggest no or weak redshift evolution of $T_{\rm dust}$ up to $z \sim 4.5$ (e.g., U. Dudzevičiūtė et al. 2020; P. M. Drew & C. M. Casey 2022; F. Sun et al. 2022), and therefore the $T_{\rm dust}(z)$ evolution at fixed stellar mass can simply be a combined effect of the weak evolution of the $L_{\rm IR}$–$T_{\rm dust}$ relation and strong evolution of the so-called star-forming "main sequence."

Nevertheless, we explore the possible $T_{\rm dust}$ range at 30–50 K, derive the $L_{\rm IR}$ for ASPIRE sources through these $T_{\rm dust}$ assumptions with the C. M. Casey (2012) SED (MBB $\beta_{\rm em} = 1.8$ and mid-IR $\alpha_{\rm MIR} = 2.0$), and plot the resultant obscured SFRD measurements in Figure 11. With hotter $T_{\rm dust}$, the resultant obscured SFRD is larger because $L_{\rm IR}$ is proportional to $T^4_{\rm dust}$ (the Stefan–Boltzmann law). However, the increase of obscured SFRD is only 0.12 dex (despite the larger uncertainty) with the assumption of $T_{\rm dust} = 50$ K, compared with the "benchmark." This is a consequence of the flattened IRLF at the faint end. Note that we also consider the CMB heating effect following E. da Cunha et al. (2013), although the effect is found to be small at $z \sim 5$ where the CMB temperature $T_{\rm CMB}$ is 16 K (the $L_{\rm IR}$ boost is $\lesssim 0.01$ dex).

We also consider the very hot IR SED template of Haro 11, a local moderately low-metallicity galaxy that undergoes starburst. M. E. De Rossi et al. (2018) suggested that the IR SED of Haro 11 could resemble those of luminous DSFGs at $z = 5-7$, many of which are quasar host galaxies (J. Lyu et al. 2017) or selected through single-dish telescopes including SPT (e.g., M. L. Strandet et al. 2016). With the Haro 11 SED assumption, all galaxies in our sample exhibit the $L_{\rm IR}$ of ULIRGs, and thus we will not be able to constrain the faint-end slope of IRLFs anymore, and literature measurements will dominate the IRLF fitting. The resultant obscured SFRD is similar to that approximated by $T_{\rm dust} = 50$ K (Figure 11).

We also derive $L_{\rm IR}$ using the $\lambda_{\rm peak}(L_{\rm IR})$ relation in C. M. Casey et al. (2018a), which is equivalent to

$$T_{\rm dust}/{\rm K} = 32.7\ [L_{\rm IR}/(10^{12}\ L_\odot)]^{0.09} \tag{5}$$

under the adopted SED assumption, and the resultant SFRD is slightly lower than our "benchmark" by 0.05 dex because of the relatively low $L_{\rm IR}$ of ASPIRE DSFGs (mostly LIRGs).

We also experiment with different assumptions of dust emissivity and rest-frame wavelength where the dust optical depth is unity, both of which were fixed in previous modeling ($\beta_{\rm em} = 1.8$ and $\lambda_{\rm thick} = 100\ \mu$m). We find that the change of $\beta_{\rm em}$ by ± 0.3 will result in a variation of 0.02 dex for $\rho_{\rm SFR,IR}$, and the change of $\lambda_{\rm thick}$ by a factor of 2 will result in a variation of 0.07 dex. These variations are relatively insignificant compared with the uncertainty of SFRD.

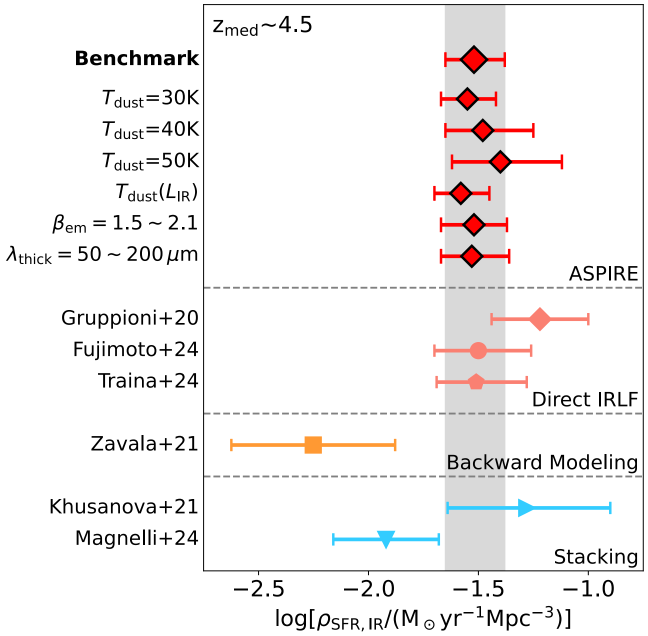

Figure 11. The 16%–50%–84% credible-interval constraints of obscured SFRD at $z\sim4.5$. Results from ASPIRE under various far-IR SED and dust temperature assumptions are shown at the top as solid red diamonds. Literature results obtained through direct measurements and the integral of the IRLF are shown as salmon-pink symbols (interpolated to $z\sim4.5$; C. Gruppioni et al. 2020; S. Fujimoto et al. 2023; A. Traina et al. 2024). The results found by J. A. Zavala et al. (2021) through backward evolutionary modeling are represented by the orange square. Results based on stacking of ALMA data in bins of stellar masses or UV luminosities are shown by cyan triangles (Y. Khusanova et al. 2021; B. Magnelli et al. 2024). The vertical gray band shows the 16%–84% credible interval of the "benchmark" obscured SFRD measured with ASPIRE.

Finally, we also consider the potential AGN contribution to the 1.2 mm ALMA continuum and thus far-IR SED. Given that we have ruled out the existence of bright point-like structures in NIRCam imaging (>27.6 AB mag at F356W, 10σ limit), any AGNs must be dust-obscured if they exist in ASPIRE DSFGs. We make use of the AGN SED templates constructed by J. Lyu et al. (2017) and J. Lyu & G. H. Rieke (2018). At the F356W detection limit, AGN at $A_V<3$ cannot contribute to more than 25% of observed ALMA flux density, and thus our SFRD measurement remains valid. However, we cannot rule out the existence of AGN with larger A_V that may contribute to the 1.2 mm flux density more significantly (e.g., M. Symeonidis et al. 2016; J. McKinney et al. 2021), although obscured AGNs are not required to interpret the observational characteristics of ASPIRE DSFGs. Obscured AGN contribution to the IR SEDs of $z=4$–6 (U)LIRGs will need to be quantified through future JWST/MIRI observations and far-IR missions.

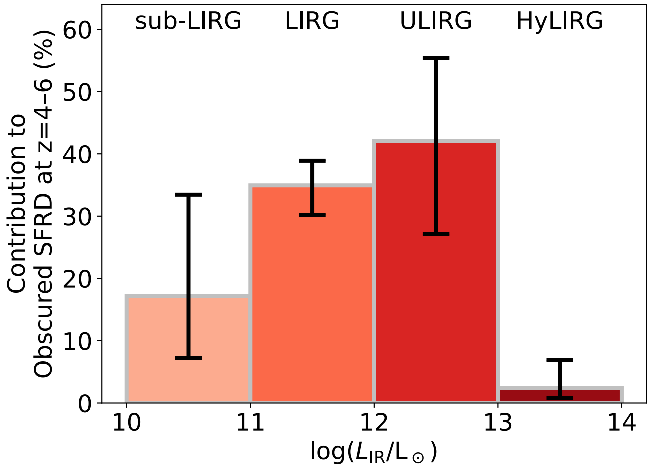

Figure 12. The contribution to the obscured cosmic SFRD at $z=4$–6 from sub-LIRGs, LIRGs, ULIRGs, and HyLIRGs at $L_{\rm IR}$ from 10^{10} to $10^{14}\,L_\odot$. LIRGs and ULIRGs at $L_{\rm IR}=10^{11}-10^{13}\,L_\odot$ contribute to the majority (81^{+11}_{-21}%) of obscured SFRD at this epoch.

In conclusion, we argue that our determination of obscured SFRD is relatively robust against largely unknown far-IR SEDs, which are only loosely constrained by ALMA photometry in just one band. The ASPIRE determinations of obscured SFRD, regardless of $T_{\rm dust}$ assumptions, are all higher than that of J. A. Zavala et al. (2021) but consistent with recent direct measurements from S. Fujimoto et al. (2023) and A. Traina et al. (2024), and exhibit smaller uncertainties than literature measurements relying on stacked ALMA data (Y. Khusanova et al. 2021; B. Magnelli et al. 2024). To further improve the accuracy of obscured SFRD determination, direct $T_{\rm dust}$ measurements through high-frequency ALMA continuum observations of $z>4$ DSFGs would be very helpful (e.g., A. L. Faisst et al. 2020; I. Mitsuhashi et al. 2024; F. Valentino et al. 2024; V. Villanueva et al. 2024).

5.2. The IRLF at the Bright End

Because of the limited survey area, our ASPIRE DSFG sample cannot constrain the IRLF at the bright end (i.e., $L_{\rm IR}>L^\star_{\rm IR}\sim10^{12.6}\,L_\odot$) in a self-contained manner. Therefore, we have to include literature measurements in our fitting, which could lead to concerns regarding $z_{\rm spec}$ completeness and $z_{\rm phot}$ validity.

Figure 12 shows the contribution to the obscured cosmic SFRD at $z=4$–6 by DSFGs in four $L_{\rm IR}$ bins, namely sub-LIRGs ($10^{10}\,L_\odot\leqslant L_{\rm IR}<10^{11}\,L_\odot$), LIRGs, ULIRGs, and HyLIRGs ($10^{13}\,L_\odot\leqslant L_{\rm IR}<10^{14}\,L_\odot$). It is evident that both LIRGs and ULIRGs contribute to the majority (81^{+11}_{-21}%) of the obscured SFRD at this epoch. However, the contribution from ULIRGs is subject to a relatively large uncertainty (44% ± 14%) because of the uncertainty of the IRLF at the bright end.

Although the spectroscopic completeness of literature measurement could be a concern, we argue that the derived $z=4$–6 IRLF in Section 8 is actually comparable to recent spectroscopic evidence. Simply considering GN10 ($z=5.30$; D. A. Riechers et al. 2020) and HDF850.1 ($z=5.18$; F. Walter et al. 2012), whose Hα lines are detected through FRESCO NIRCam WFSS in the F444W band (F. Sun et al. 2024; see also M. Xiao et al. 2024; T. Herard-Demanche et al. 2025), we can roughly estimate a volume density of $\Phi=10^{-5.0\pm0.4}\,{\rm Mpc^{-3}\ dex^{-1}}$ (cosmic variance considered) within the luminosity bin $10^{12.5}-10^{13.1}\,L_\odot$, assuming the FRESCO survey volume at $z=4.9-6.0$. This is consistent with the volume density expected from our best-fit IRLF at the bin center ($\Phi=10^{-5.4}\,{\rm Mpc^{-3}\ dex^{-1}}$). However, we also note that both galaxies reside in a complex overdense environment (R. Calvi et al. 2021, 2023; F. Sun et al. 2024; T. Herard-Demanche et al. 2025), and there could be more galaxies in both GOODS fields that could contribute to the volume density (M. Xiao et al. 2024).

In JWST Cycle-3, there are four planned large/treasury NIRCam WFSS surveys over much larger volumes, including NEXUS (PID: 5105, PI: Y. Shen.; Y. Shen et al. 2024), COSMOS-3D (PID: 5893, PI: K. Kakiichi), POPPIES (PID:

5398, PI: J. Kartaltepe), and SAPPHIRES (PID: 6434, PI: E. Egami), totaling more than 1,000 hours of JWST time. These observations, in synergy with obtained / planned (sub) millimeter surveys in cosmological deep fields such as COSMOS (C. M. Casey et al. 2013, 2021; J. E. Geach et al. 2017; W.-H. Wang et al. 2017; J. M. Simpson et al. 2019) and NEP (H. Shim et al. 2020; M. Hyun et al. 2023), will provide powerful and essential spectroscopy of high-redshift DSFGs at the bright end of the IRLF,4constraining the obscured cosmic star formation history toward the Epoch of Reionization with unprecedented accuracy.

6. Summary

In this paper, we present a stringent measurement of the dust-obscured SFRD at $z = 4$–6 through the ASPIRE JWST and ALMA survey. ASPIRE obtained JWST NIRCam WFSS survey at 3.1–4.0 μm and ALMA mosaics at 1.2 mm along 25 quasar sightlines. We make use of this JWST and ALMA data set to identify DSFGs at $z_{\rm spec} = 4-6$ through ALMA continuum detections and JWST spectroscopy. The main results are summarized as follows:

1. We identify eight DSFGs at $z_{\rm spec} = 4-6$ through the detections of Hα (for seven sources at $z = 4.07-4.80$) or [O III] λ5008 (for one source at $z = 5.55$) lines with NIRCam WFSS. These DSFGs are discovered in seven out of 25 ASPIRE quasar fields totaling a survey area of ∼35 arcmin^2. For six DSFGs, we also detect at least one more faint lines such as Hβ, [O III] λ4960, [N II] λ6585, and [S II] $\lambda\lambda$6718,6733.
2. We conduct energy-balance SED modeling of these DSFGs through JWST and ALMA photometry (four bands in total). The median stellar mass is $\log(M_{\rm star}/M_\odot) = 10.3 \pm 0.2$, and the median IR luminosity is $\log(L_{\rm IR}/L_\odot) = 11.7 \pm 0.1$.
3. We find 96% ± 2% of the star formation in $z \sim 5$ DSFGs probed by ASPIRE to be obscured by dust. However, the escape fractions of Hα photons are anticorrelated with their IR luminosities, resulting in an almost constant Hα luminosity across a 2 dex wide span of $L_{\rm IR}$, which is also well above the 5σ detection limit with NIRCam WFSS. We observe a typical $\tau_{\rm UV}/\tau_{\rm H\alpha}$ ratio of 1.61 ± 0.34 for $z \sim 5$ DSFGs, slightly higher than that of a local starburst, which could lead to an enhanced Hα visibility in these $z \sim 5$ DSFGs.
4. We obtain a 1.2 mm number count of DSFGs at $z = 4$–6, finding it to be higher than a previous determination based on the ALMA Cycle-4 large program ASPECS (G. Popping et al. 2020; J. A. Zavala et al. 2021) but similar to that from the ALMA Cycle-5 large program ALPINE (C. Gruppioni et al. 2020). We argue that our measurement is robust against cosmic variance (shot noise) because of averaging 25 independent sightlines, while the ASPECS survey in the HUDF region encounters a void of DSFGs at $z = 4$–6 because of strong shot noise.
5. We obtain spectroscopically complete measurement of the IRLF at $z = 4$–6 down to $L_{\rm IR} \sim 2 \times 10^{11}\,L_\odot$. We observe a flattening of the faint-end slope ($\alpha = 0.59^{+0.39}_{-0.45}$) of the IRLF. Our measurements are consistent with previous measurements, including those of C. Gruppioni et al. (2020), S. Fujimoto et al. (2023), and A. Traina et al. (2024) at the faint end (with spectroscopic incompleteness), but slightly lower than a few model predictions.
6. We derive an obscured SFRD of $\log[\rho_{\rm SFR,IR}/(M_\odot\,{\rm yr}^{-1}{\rm Mpc}^{-3})] = -1.52^{+0.14}_{-0.13}$ at $z = 4$–6 (median $z =$;4.5). This is comparable to the total (obscured and unobscured) SFRD modeled by P. Madau & M. Dickinson (2014), suggesting that the majority (66^{+7}_{-7}%) of the total SFRD is obscured by dust at this epoch. Our measurement is similar to that of direct measurements with recent literature (e.g., S. Fujimoto et al. 2023; A. Traina et al. 2024), but ∼ 5 times higher than that obtained by J. A. Zavala et al. (2021) through a backward evolutionary modeling.
7. We conclude that our measurement of SFRD is relatively robust against uncertainty in far-IR SED shape (primarily dust temperature). Future ALMA high-frequency observations will be helpful to determine the dust temperature and improve the accuracy of obscured SFRD. Although our result suggests the majority (81^{+11}_{-21}%) of obscured SFRD is contributed by both LIRGs and ULIRGs, the current uncertainty at the bright end of IRLF (especially $z_{\rm spec}$ incompleteness) will need to be resolved with planned JWST NIRCam WFSS surveys over much larger volumes.

Acknowledgments

We thank JWST #2078 program coordinator Weston Eck and ALMA program #2022.1.01077.L contact scientist Catherine Vlahakis for their support of our observing programs. We thank NRAO for providing computational resource support for ALMA data processing. We thank the anonymous referee for helpful comments. F.S. thanks Seiji Fujimoto for helpful discussions.

F.S. acknowledges funding from JWST/NIRCam contract to the University of Arizona, NAS5-02105 and support for JWST program #2883 provided by NASA through a grant from the Space Telescope Science Institute, which is operated by the Association of Universities for Research in Astronomy, Inc., under NASA contract NAS 5-03127. F.W. and X.F. acknowledge support from NSF Grant AST-2308258. J.B.C. acknowledges funding from the JWST Arizona/Steward Postdoc in Early galaxies and Reionization (JASPER) Scholar contract at the University of Arizona. L.C. acknowledges support by grant PIB2021-127718NB-100 from the Spanish Ministry of Science and Innovation/State Agency of Research MCIN/AEI/10.13039/501100011033 and by “ERDF A way of making Europe.” Y.K. thanks the support of the German Space Agency (DLR) through the program LEGACY 50OR2303. R.A.M. acknowledges support from the Swiss National Science Foundation (SNSF) through project grant 200020_207349. S. Z. acknowledges support from the National Science Foundation of China (no. 12303011).

This paper makes use of the following ALMA data: ADS/JAO.ALMA#2022.1.01077.L. ALMA is a partnership of ESO (representing its member states), NSF (USA), and NINS (Japan), together with NRC (Canada), MOST and ASIAA (Taiwan), and KASI (Republic of Korea), in cooperation with the Republic of Chile. The Joint ALMA Observatory is operated by ESO, AUI/NRAO, and NAOJ. The National

Radio Astronomy Observatory is a facility of the National Science Foundation operated under cooperative agreement by Associated Universities, Inc.

This work is based on observations made with the NASA/ESA/CSA James Webb Space Telescope. The data were obtained from the Mikulski Archive for Space Telescopes at the Space Telescope Science Institute, which is operated by the Association of Universities for Research in Astronomy, Inc., under NASA contract NAS 5-03127 for JWST. These observations are associated with program #2078. The JWST data presented in this paper were obtained from the Mikulski Archive for Space Telescopes (MAST) at the Space Telescope Science Institute. The specific observations analyzed can be accessed via doi:10.17909/vt74-kd84. Support for program #2078 was provided by NASA through a grant from the Space Telescope Science Institute, which is operated by the Association of Universities for Research in Astronomy, Inc., under NASA contract NAS 5-03127.

Facilities: JWST (NIRCam), ALMA.

Software: ASTROPY (Astropy Collaboration et al. 2013, 2018), CASA (J. P. McMullin et al. 2007; CASA Team et al. 2022), CIGALE (S. Noll et al. 2009; M. Boquien et al. 2019), EMCEE (D. Foreman-Mackey et al. 2013), GALFIT (C. Y. Peng et al. 2010), JWST (H. Bushouse et al. 2023), LENSTOOL (E. Jullo et al. 2007), PHOTUTILS (L. Bradley et al. 2024), WEBBPSF (M. D. Perrin et al. 2014),

Appendix A
Lensing Magnification

The highest-redshift source in our sample, J0109m3047.C02 ($z = 5.549$) is very close to a foreground galaxy (separation $\sim 0\farcs8$). J0109m3047.C02 is also extended in morphology along the tangential direction to this foreground galaxy, indicating that J0109m3047.C02 is strongly lensed by the foreground source. To correctly account for the lensing effect in the analyses of its physical properties and lensing bias in the determination of LF, we model the lensing magnification through the following steps.

We first obtain optical and near-IR photometry of the foreground lens. At optical wavelengths, the foreground galaxy is much brighter than J0109m3047.C02 and the other bluer source to the northwest, as seen in Figure 2. Therefore, we directly make use of DES DR2 (T. M. C. Abbott et al. 2021) photometry in the g, r, i, z, and Y bands. At JWST/NIRCam wavelength, we carefully model the source morphology with GALFIT (C. Y. Peng et al. 2010). Because J0109m3047.C02 appears clumpy in the image, we include 10 components of Sérsic profiles or point-spread functions (PSFs) to model the complex image in the F115W, F200W, and F356W bands. We make use of a PSF model generated through WEBBPSF (M. D. Perrin et al. 2014). Except for the foreground lens component, the best-fit morphological models of other components are subtracted from the mosaicked images. We therefore obtain the near-IR aperture photometry of the foreground lens on the residual images (22.90 ± 0.05, 21.82 ± 0.04, and 21.12 ± 0.05 AB mag in the F115W, F200W, and F356W bands, respectively).

Because no obvious emission or absorption line could be identified in the grism spectra of the foreground lens, we derive the photometric redshifts through SED modeling. We feed the photometric measurements into CIGALE (M. Boquien et al. 2019) with redshift grids from $z = 0.5$ to 2.5 ($\Delta z = 0.05$), and derive the reduced $\chi^2_{\rm red}(z)$ and stellar mass $M_{\rm star}(z)$ for each of the fitting. We derive the probability distribution of redshifts through $P(z) \propto \exp[-\chi^2_{\rm red}(z)/2]$ and normalization $\int_{0.5}^{2.5} P(z)dz = 1$, and conclude a photometric redshift of $z_{\rm phot} = 1.18 \pm 0.05$ for the foreground lens. At this redshift, no strong hydrogen line is expected in the F356W grism spectrum, consistent with the aforementioned nondetection. We randomly draw redshifts from the $P(z)$ distribution, and then draw the corresponding $M_{\rm star}$ from the best-fit $M_{\rm star}(z)$ and the uncertainties. Assuming the stellar-mass Tully–Fisher Relation measured at $z \sim 1$ (H. Übler et al. 2017), we derive the velocity dispersion (σ_v) for each of the drawn pairs of z and $M_{\rm star}$. The median and 1σ uncertainty of velocity dispersion is $\sigma_v = 150 \pm 28\,{\rm km\,s^{-1}}$ for the foreground lens.

We then model the foreground lens using the drawn redshifts and σ_v through the LENSTOOL (E. Jullo et al. 2007) software. We assume a singular isothermal spherical distribution of matter in the foreground potential. We therefore derive a lensing magnification of $\mu = 1.91 \pm 0.50$ for the ALMA continuum source. However, we note that the differential lensing effect is seen for J0109m3047.C02 because of its complex morphology at different wavelengths. The light-weighted (through image segments) magnifications for J0109m3047.C02 in the F115W, F200W, and F356W bands are 1.58 ± 0.33, 1.54 ± 0.29 and 1.53 ± 0.28, respectively. These magnification factors have been corrected when we infer the physical properties (e.g., luminosity and mass) of J0109m3047.C02.

Appendix B
Completeness Correction

We simulate ALMA observations with CASA to derive the completeness correction at each ALMA source flux and S/N. First of all, we assume a 2D circular Gaussian profile for each ALMA continuum source with an effective radius $R_{\rm e} = 0\farcs23$ (i.e., 1.5 kpc at $z = 4.5$). This is consistent with the sizes that we measured from image-plane fitting (with CASA `imfit`) for ASPIRE DSFGs detected at $z = 4$–6 and S/N > 10. We scale the surface brightness profile such that the total flux density is 0.10–1.0 mJy at 1.2 mm in each run of our simulations. ALMA continuum observation measurement sets are then simulated via the CASA `simobserve` command, with an identical configuration and similar observing conditions (exposure time and precipitated water vapor) to those of actual ASPIRE observations. With each input flux density, we simulate the observations 100 times, produce the continuum images at both native and a $1\farcs0$-tapered resolution with the same pipeline as that adopted for real data. We then identify peaks in simulated images within $1''$ from the injected source position. The detection criteria are the same as those adopted in Section 2.2.

At each injected source flux density, we compute the fraction of sources in simulated images that are above our detection threshold. Such a fraction is therefore considered to be the survey completeness at the injected source flux, and Figure B1 shows the completeness as a function of ALMA flux density on the tapered images. We also conduct statistics on native-resolution images, but the results are less relevant because all of the ASPIRE DSFGs $z = 4$–6 exhibit higher S/N on tapered images than native images (and thus completeness is higher).

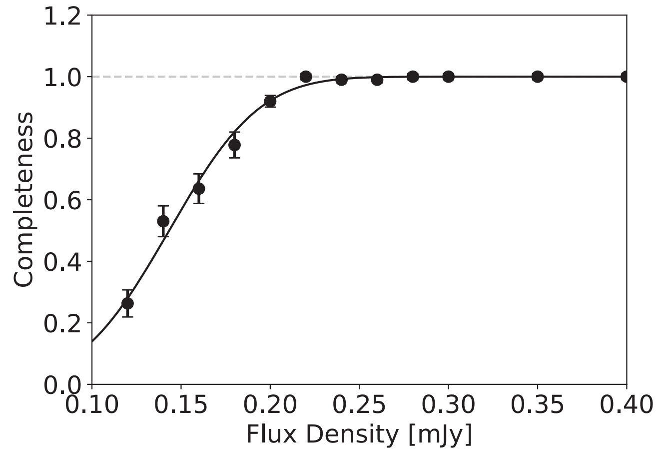

Figure B1. Completeness as a function of ALMA flux density on $1\farcs0$ uv-tapered images (before primary beam response correction). The best-fit error function is shown as a solid black line.

We fit the measured completeness with an error function:

$$C(f) = \frac{1}{2}\mathrm{erf}(\frac{S - S_0}{\sigma}) + \frac{1}{2}, \tag{B1}$$

and we find that the completeness is 50% at source flux density $S = S_0 = 0.143 \pm 0.003$ mJy. All ASPIRE DSFGs at $z = 4$–6 show high completeness ($C \sim 1$) because of their high fidelity of detections ($S_{1.2\,\mathrm{mm}} \geqslant 0.24$ mJy and S/N⩾6.5). We also rewrite the completeness function in terms of ALMA source S/N and use it for the IRLF completeness calculation.

Through our injection and detection experiment, we also verify the 1.1× scaling factor applied to the peak flux density measured on the tapered image (f_{tap}; Section 3.1). We also conclude there is a negligible flux boosting effect (e.g., Eddington bias; <3% through our simulations) in the S/N and flux density range of our targets.

ORCID iDs

Fengwu Sun https://orcid.org/0000-0002-4622-6617
Feige Wang https://orcid.org/0000-0002-7633-431X
Jinyi Yang https://orcid.org/0000-0001-5287-4242
Jaclyn B. Champagne https://orcid.org/0000-0002-6184-9097
Roberto Decarli https://orcid.org/0000-0002-2662-8803
Xiaohui Fan https://orcid.org/0000-0003-3310-0131
Eduardo Bañados https://orcid.org/0000-0002-2931-7824
Zheng Cai https://orcid.org/0000-0001-8467-6478
Luis Colina https://orcid.org/0000-0002-9090-4227
Eiichi Egami https://orcid.org/0000-0003-1344-9475
Joseph F. Hennawi https://orcid.org/0000-0002-7054-4332
Xiangyu Jin https://orcid.org/0000-0002-5768-738X
Hyunsung D. Jun https://orcid.org/0000-0003-1470-5901
Yana Khusanova https://orcid.org/0000-0002-7220-397X
Mingyu Li https://orcid.org/0000-0001-6251-649X
Zihao Li https://orcid.org/0000-0001-5951-459X
Xiaojing Lin https://orcid.org/0000-0001-6052-4234
Weizhe Liu https://orcid.org/0000-0003-3762-7344
Romain A. Meyer https://orcid.org/0000-0001-5492-4522
Maria A. Pudoka https://orcid.org/0000-0003-4924-5941
George H. Rieke https://orcid.org/0000-0003-2303-6519
Yue Shen https://orcid.org/0000-0003-1659-7035
Wei Leong Tee https://orcid.org/0000-0003-0747-1780
Bram Venemans https://orcid.org/0000-0001-9024-8322
Fabian Walter https://orcid.org/0000-0003-4793-7880
Yunjing Wu https://orcid.org/0000-0003-0111-8249
Huanian Zhang https://orcid.org/0000-0002-0123-9246
Siwei Zou https://orcid.org/0000-0002-3983-6484

References

Abbott, T. M. C., Adamów, M., Aguena, M., et al. 2021, ApJS, 255, 20
Adscheid, S., Magnelli, B., Liu, D., et al. 2024, A&A, 685, A1
Alavi, A., Siana, B., Richard, J., et al. 2016, ApJ, 832, 56
Alcalde Pampliega, B., Pérez-González, P. G., Barro, G., et al. 2019, ApJ, 876, 135
Algera, H. S. B., Inami, H., Oesch, P. A., et al. 2023, MNRAS, 518, 6142
Aravena, M., Boogaard, L., Gónzalez-López, J., et al. 2020, ApJ, 901, 79
Armus, L., Mazzarella, J. M., Evans, A. S., et al. 2009, PASP, 121, 559
Arnouts, S., & Ilbert, O., 2011 LePHARE: Photometric Analysis for Redshift Estimate, Astrophysics Source Code Library, ascl:1108.009
Astropy Collaboration, Price-Whelan, A. M., Sipőcz, B. M., et al. 2018, AJ, 156, 123
Astropy Collaboration, Robitaille, T. P., Tollerud, E. J., et al. 2013, A&A, 558, A33
Bañados, E., Mazzucchelli, C., Momjian, E., et al. 2021, ApJ, 909, 80
Barrufet, L., Oesch, P., Marques-Chaves, R., et al. 2025, MNRAS, in press (doi:10.1093/mnras/staf013)
Bauer, F. E., Alexander, D. M., Brandt, W. N., et al. 2004, AJ, 128, 2048
Béthermin, M., Fudamoto, Y., Ginolfi, M., et al. 2020, A&A, 643, A2
Béthermin, M., Gkogkou, A., Van Cuyck, M., et al. 2022, A&A, 667, A156
Béthermin, M., Wu, H.-Y., Lagache, G., et al. 2017, A&A, 607, A89
Bik, A., Álvarez-Márquez, J., Colina, L., et al. 2024, A&A, 686, A3
Boogaard, L. A., Gillman, S., Melinder, J., et al. 2024, ApJ, 969, 27
Boquien, M., Burgarella, D., Roehlly, Y., et al. 2019, A&A, 622, A103
Bouwens, R., González-López, J., Aravena, M., et al. 2020, ApJ, 902, 112
Bouwens, R. J., Illingworth, G. D., Oesch, P. A., et al. 2015, ApJ, 811, 140
Bradley, L., Sipőcz, B., Robitaille, T., et al. 2024, astropy/photutils: v1.12.0, Zenodo, doi:10.5281/zenodo.10967176
Bruzual, G., & Charlot, S. 2003, MNRAS, 344, 1000
Burgarella, D., Buat, V., Gruppioni, C., et al. 2013, A&A, 554, A70
Bushouse, H., Eisenhamer, J., Dencheva, N., et al. 2023, JWST Calibration Pipeline, v1.10.2, Zenodo, doi:10.5281/zenodo.7829329
Calvi, R., Castignani, G., & Dannerbauer, H. 2023, A&A, 678, 15
Calvi, R., Dannerbauer, H., Arrabal Haro, P., et al. 2021, MNRAS, 502, 4558
Calzetti, D. 1997, in AIP Conf. Ser. 408, The Ultraviolet Universe at Low and High Redshift, ed. W. H. Waller (Melville, NY: AIP), 403
Calzetti, D., Armus, L., Bohlin, R. C., et al. 2000, ApJ, 533, 682
Caputi, K. I., Dunlop, J. S., McLure, R. J., et al. 2012, ApJL, 750, L20
CASA Team, Bean, B., Bhatnagar, S., et al. 2022, PASP, 134, 114501
Casey, C. M. 2012, MNRAS, 425, 3094
Casey, C. M., Chen, C.-C., Cowie, L. L., et al. 2013, MNRAS, 436, 1919
Casey, C. M., Hodge, J., Zavala, J. A., et al. 2018a, ApJ, 862, 78
Casey, C. M., Narayanan, D., & Cooray, A. 2014a, PhR, 541, 45
Casey, C. M., Scoville, N. Z., Sanders, D. B., et al. 2014b, ApJ, 796, 95
Casey, C. M., Zavala, J. A., Aravena, M., et al. 2019, ApJ, 887, 55
Casey, C. M., Zavala, J. A., Manning, S. M., et al. 2021, ApJ, 923, 215
Casey, C. M., Zavala, J. A., Spilker, J., et al. 2018b, ApJ, 862, 77
Chabrier, G. 2003, PASP, 115, 763
Champagne, J. B., Wang, F., Yang, J., et al. 2024a, arXiv:2410.03827
Champagne, J. B., Wang, F., Zhang, H., et al. 2024b, arXiv:2410.03826
Chary, R., & Elbaz, D. 2001, ApJ, 556, 562
Chen, C.-C., Liao, C.-L., Smail, I., et al. 2022, ApJ, 929, 159
Chen, J., Ivison, R. J., Zwaan, M. A., et al. 2023, MNRAS, 518, 1378
Colina, L., Crespo Gómez, A., Álvarez-Márquez, J., et al. 2023, A&A, 673, L6
Cooper, O. R., Brammer, G., Heintz, K. E., et al. 2024, arXiv:2410.08387
Cowie, L. L., Garmire, G. P., Bautz, M. W., et al. 2002, ApJL, 566, L5
Cucciati, O., Tresse, L., Ilbert, O., et al. 2012, A&A, 539, A31
da Cunha, E., Groves, B., Walter, F., et al. 2013, ApJ, 766, 13
da Cunha, E., Walter, F., Smail, I. R., et al. 2015, ApJ, 806, 110
De Rossi, M. E., Rieke, G. H., Shivaei, I., Bromm, V., & Lyu, J. 2018, ApJ, 869, 4
Decarli, R., Walter, F., Venemans, B. P., et al. 2017, Natur, 545, 457
Dey, A., Schlegel, D. J., Lang, D., et al. 2019, AJ, 157, 168
Drew, P. M., & Casey, C. M. 2022, ApJ, 930, 142
Driver, S. P., & Robotham, A. S. G. 2010, MNRAS, 407, 2131
Dudzevičiūtė, U., Smail, I., Swinbank, A. M., et al. 2020, MNRAS, 494, 3828
Dunlop, J. S., McLure, R. J., Biggs, A. D., et al. 2017, MNRAS, 466, 861

Enia, A., Talia, M., Pozzi, F., et al. 2022, ApJ, 927, 204

Faisst, A. L., Fudamoto, Y., Oesch, P. A., et al. 2020, MNRAS, 498, 4192

Finkelstein, S. L., Ryan, Russell E., J., Papovich, C., et al. 2015, ApJ, 810, 71

Foreman-Mackey, D., Hogg, D. W., Lang, D., & Goodman, J. 2013, PASP, 125, 306

Franco, M., Elbaz, D., Béthermin, M., et al. 2018, A&A, 620, A152

Fudamoto, Y., Oesch, P. A., Faisst, A., et al. 2020, A&A, 643, A4

Fudamoto, Y., Oesch, P. A., Schouws, S., et al. 2021, Natur, 597, 489

Fujimoto, S., Ouchi, M., Ono, Y., et al. 2016, ApJS, 222, 1

Fujimoto, S., Kohno, K., Ouchi, M., et al. 2023, ApJS, 275, 36

Gaia Collaboration, Vallenari, A., Brown, A. G. A., et al. 2023, A&A, 674, A1

Garcìa-Marìn, M., Colina, L., & Arribas, S. 2009, A&A, 505, 1017

Gardner, J. P., Mather, J. C., Abbott, R., et al. 2023, PASP, 135, 068001

Geach, J. E., Dunlop, J. S., Halpern, M., et al. 2017, MNRAS, 465, 1789

Gehrels, N. 1986, ApJ, 303, 336

Giménez-Arteaga, C., Brammer, G. B., Marchesini, D., et al. 2022, ApJS, 263, 17

Gómez-Guijarro, C., Elbaz, D., Xiao, M., et al. 2022, A&A, 658, A43

González-López, J., Novak, M., Decarli, R., et al. 2020, ApJ, 897, 91

Gordon, K. D., Clayton, G. C., Misselt, K. A., Landolt, A. U., & Wolff, M. J. 2003, ApJ, 594, 279

Gottumukkala, R., Barrufet, L., Oesch, P. A., et al. 2024, MNRAS, 530, 966

Gruppioni, C., Béthermin, M., Loiacono, F., et al. 2020, A&A, 643, A8

Gruppioni, C., Pozzi, F., Rodighiero, G., et al. 2013, MNRAS, 432, 23

Hatsukade, B., Kohno, K., Yamaguchi, Y., et al. 2018, PASJ, 70, 105

Herard-Demanche, T., Bouwens, R. J., Oesch, P. A., et al. 2025, MNRAS, in press (doi:10.1093/mnras/staf030)

Hodge, J. A., & da Cunha, E. 2020, RSOS, 7, 200556

Horne, K. 1986, PASP, 98, 609

Huang, J. S., Zheng, X. Z., Rigopoulou, D., et al. 2011, ApJL, 742, L13

Hughes, D. H., Serjeant, S., Dunlop, J., et al. 1998, Natur, 394, 241

Hyun, M., Im, M., Smail, I. R., et al. 2023, ApJS, 264, 19

Jin, J.-J., Zhu, Y.-N., Wu, H., et al. 2019, ApJS, 244, 33

Jin, S., Daddi, E., Magdis, G. E., et al. 2019, ApJ, 887, 144

Jin, S., Sillassen, N. B., Hodge, J., et al. 2024, A&A, 690L, L16

Jin, X., Yang, J., Fan, X., et al. 2024, ApJ, 976, 93

Jullo, E., Kneib, J. P., Limousin, M., et al. 2007, NJPh, 9, 447

Kennicutt, R. C. J. 1998, ARA&A, 36, 189

Kepley, A. A., Tsutsumi, T., Brogan, C. L., et al. 2020, PASP, 132, 024505

Khusanova, Y., Bethermin, M., Le Fèvre, O., et al. 2021, A&A, 649, A152

Kohno, K., Fujimoto, S., Tsujita, A., et al. 2023, in Proc. of the 7th Chile-Cologne-Bonn Symp., Physics and Chemistry of Star Formation: The Dynamical ISM Across Time and Spatial Scales, ed. V. Ossenkopf-Okada et al. (Universitäts- und Stadtbibliothekj Köln), 16

Kokorev, V., Brammer, G., Fujimoto, S., et al. 2022, ApJS, 263, 38

Koprowski, M. P., Dunlop, J. S., Michałowski, M. J., et al. 2017, MNRAS, 471, 4155

Lagos, C. d. P., da Cunha, E., Robotham, A. S. G., et al. 2020, MNRAS, 499, 1948

Le Fèvre, O., Béthermin, M., Faisst, A., et al. 2020, A&A, 643, A1

Lim, C.-F., Wang, W.-H., Smail, I., et al. 2020, ApJ, 889, 80

Ling, C., Sun, B., Cheng, C., et al. 2024, ApJL, 969, 28

Liu, D., Daddi, E., Dickinson, M., et al. 2018, ApJ, 853, 172

Lyu, J., & Rieke, G. H. 2018, ApJ, 866, 92

Lyu, J., Rieke, G. H., & Shi, Y. 2017, ApJ, 835, 257

Madau, P., & Dickinson, M. 2014, ARA&A, 52, 415

Magnelli, B., Adscheid, S., Wang, T.-M., et al. 2024, A&A, 688, 55

Magnelli, B., Lutz, D., Saintonge, A., et al. 2014, A&A, 561, A86

Manning, S. M., Casey, C. M., Zavala, J. A., et al. 2022, ApJ, 925, 23

Mazzucchelli, C., Decarli, R., Farina, E. P., et al. 2019, ApJ, 881, 163

McKinney, J., Casey, C. M., Long, A. S., et al. 2024, arXiv:2408.08346

McKinney, J., Finnerty, L., Casey, C. M., et al. 2023a, ApJL, 946, L39

McKinney, J., Hayward, C. C., Rosenthal, L. J., et al. 2021, ApJ, 921, 55

McKinney, J., Manning, S. M., Cooper, O. R., et al. 2023b, ApJ, 956, 72

McMullin, J. P., Waters, B., Schiebel, D., Young, W., & Golap, K. 2007, in ASP Conf. Ser. 376, Astronomical Data Analysis Software and Systems XVI, ed. R. A. Shaw, F. Hill, & D. J. Bell (San Francisco, CA: ASP), 127

Mehta, V., Scarlata, C., Rafelski, M., et al. 2017, ApJ, 838, 29

Meurer, G. R., Heckman, T. M., & Calzetti, D. 1999, ApJ, 521, 64

Mitsuhashi, I., Harikane, Y., Bauer, F. E., et al. 2024, ApJ, 971, 161

Moretti, A., Campana, S., Lazzati, D., & Tagliaferri, G. 2003, ApJ, 588, 696

Moster, B. P., Somerville, R. S., Newman, J. A., & Rix, H.-W. 2011, ApJ, 731, 113

Moutard, T., Sawicki, M., Arnouts, S., et al. 2020, MNRAS, 494, 1894

Nguyen, H. T., Schulz, B., Levenson, L., et al. 2010, A&A, 518, L5

Noll, S., Burgarella, D., Giovannoli, E., et al. 2009, A&A, 507, 1793

Oesch, P. A., Brammer, G., Naidu, R. P., et al. 2023, MNRAS, 525, 2864

Oesch, P. A., Stiavelli, M., Carollo, C. M., et al. 2007, ApJ, 671, 1212

Oke, J. B., & Gunn, J. E. 1983, ApJ, 266, 713

Oteo, I., Cepa, J., Bongiovanni, Á., et al. 2013, A&A, 554, L3

Peng, C. Y., Ho, L. C., Impey, C. D., & Rix, H.-W. 2010, AJ, 139, 2097

Penner, K., Dickinson, M., Pope, A., et al. 2012, ApJ, 759, 28

Pereira-Santaella, M., Alonso-Herrero, A., Colina, L., et al. 2015, A&A, 577, A78

Perrin, M. D., Sivaramakrishnan, A., Lajoie, C.-P., et al. 2014, Proc. SPIE, 9143, 91433X

Popping, G., Walter, F., Behroozi, P., et al. 2020, ApJ, 891, 135

Prochaska, J., Hennawi, J., Westfall, K., et al. 2020, JOSS, 5, 2308

Rawle, T. D., Egami, E., Bussmann, R. S., et al. 2014, ApJ, 783, 59

Reddy, N. A., & Steidel, C. C. 2009, ApJ, 692, 778

Reuter, C., Vieira, J. D., Spilker, J. S., et al. 2020, ApJ, 902, 78

Riechers, D. A., Bradford, C. M., Clements, D. L., et al. 2013, Natur, 496, 329

Riechers, D. A., Hodge, J. A., Pavesi, R., et al. 2020, ApJ, 895, 81

Rieke, G. H., Alonso-Herrero, A., Weiner, B. J., et al. 2009, ApJ, 692, 556

Rieke, M. J., Kelly, D. M., Misselt, K., et al. 2023, PASP, 135, 028001

Rowan-Robinson, M., Oliver, S., Wang, L., et al. 2016, MNRAS, 461, 1100

Schmidt, M. 1968, ApJ, 151, 393

Schreiber, C., Elbaz, D., Pannella, M., et al. 2018, A&A, 609, A30

Shen, Y., Zhuang, M.-Y., Li, J., et al. 2024, arXiv:2408.12713

Shim, H., Kim, Y., Lee, D., et al. 2020, MNRAS, 498, 5065

Simpson, J. M., Smail, I., Swinbank, A. M., et al. 2015, ApJ, 799, 81

Simpson, J. M., Smail, I., Swinbank, A. M., et al. 2019, ApJ, 880, 43

Strandet, M. L., Weiss, A., Vieira, J. D., et al. 2016, ApJ, 822, 80

Sun, F., Egami, E., Fujimoto, S., et al. 2022, ApJ, 932, 77

Sun, F., Egami, E., Pérez-González, P. G., et al. 2021, ApJ, 922, 114

Sun, F., Egami, E., Pirzkal, N., et al. 2023, ApJ, 953, 53

Sun, F., Helton, J. M., Egami, E., et al. 2024, ApJ, 961, 69

Sun, L., Wang, X., Teplitz, H. I., et al. 2023, ApJ, 972, 8

Symeonidis, M., Giblin, B. M., Page, M. J., et al. 2016, MNRAS, 459, 257

Tacchella, S., Eisenstein, D. J., Hainline, K., et al. 2023, ApJ, 952, 74

Talia, M., Cimatti, A., Giulietti, M., et al. 2021, ApJ, 909, 23

Traina, A., Gruppioni, C., Delvecchio, I., et al. 2024, A&A, 681, A118

Trayford, J. W., Lagos, C. d. P., Robotham, A. S. G., & Obreschkow, D. 2020, MNRAS, 491, 3937

Trenti, M., & Stiavelli, M. 2008, ApJ, 676, 767

Tsujita, A., Kohno, K., Huang, S., et al. 2024, arXiv:2406.09890

Übler, H., D'Eugenio, F., Perna, M., et al. 2024, MNRAS, 533, 4287

Übler, H., Förster Schreiber, N. M., Genzel, R., et al. 2017, ApJ, 842, 121

Valentino, F., Fujimoto, S., Giménez-Arteaga, C., et al. 2024, A&A, 685, A138

Venemans, B. P., Neeleman, M., Walter, F., et al. 2019, ApJL, 874, L30

Vijayan, A. P., Wilkins, S. M., Lovell, C. C., et al. 2022, MNRAS, 511, 4999

Villanueva, V., Herrera-Camus, R., Gonzalez-Lopez, J., et al. 2024, A&A, 691, A133

Walter, F., Decarli, R., Aravena, M., et al. 2016, ApJ, 833, 67

Walter, F., Decarli, R., Carilli, C., et al. 2012, Natur, 486, 233

Wang, F., Yang, J., Hennawi, J. F., et al. 2023, ApJL, 951, L4

Wang, L., Pearson, W. J., Cowley, W., et al. 2019, A&A, 624, A98

Wang, T., Elbaz, D., Schreiber, C., et al. 2016, ApJ, 816, 84

Wang, T., Schreiber, C., Elbaz, D., et al. 2019, Natur, 572, 211

Wang, W.-H., Lin, W.-C., Lim, C.-F., et al. 2017, ApJ, 850, 37

Weiß, A., De Breuck, C., Marrone, D. P., et al. 2013, ApJ, 767, 88

Whitaker, K. E., Pope, A., Cybulski, R., et al. 2017, ApJ, 850, 208

Williams, C. C., Alberts, S., Ji, Z., et al. 2024, ApJ, 968, 34

Williams, C. C., Labbe, I., Spilker, J., et al. 2019, ApJ, 884, 154

Wu, Y., Wang, F., Cai, Z., et al. 2023, ApJL, 956, L40

Xiao, M. Y., Elbaz, D., Gómez-Guijarro, C., et al. 2023, A&A, 672, A18

Xiao, M., Oesch, P., Elbaz, D., et al. 2024, Natur, 635, 311

Yamaguchi, Y., Kohno, K., Hatsukade, B., et al. 2019, ApJ, 878, 73

Yang, J., Wang, F., Fan, X., et al. 2021, ApJ, 923, 262

Yang, J., Wang, F., Fan, X., et al. 2023, ApJL, 951, L5

Zavala, J. A., Casey, C. M., Manning, S. M., et al. 2021, ApJ, 909, 165

Zimmerman, D. T., Narayanan, D., Whitaker, K. E., & Davé, R. 2024, ApJ, 973, 146

Zou, S., Cai, Z., Wang, F., et al. 2024, ApJL, 963, L28